First-principles and Theoretical Analysis of Electronic, Optical and Vibrational Properties in Layered Materials

A Thesis

Submitted in fulfilment for the Degree of

Master of Science

by

Sarbajit Dutta

Chemistry and Physics of Materials Unit
Jawaharlal Nehru Centre for Advanced Scientific Research
Bengaluru-560064

March 2023

To my parents

DECLARATION

I hereby declare that the matter embodied in the thesis entitled "**First-principles and Theoretical Analysis of Electronic, Optical and Vibrational Properties in Layered Materials**" is the result of investigations carried out by me at the Chemistry and Physics of Materials Unit, Jawaharlal Nehru Centre for Advanced Scientific Research, Bangalore, India under the supervision of Prof. Umesh V. Waghmare and that it has not been submitted elsewhere for the award of any degree or diploma.

In keeping with the general practice in reporting scientific observations, due acknowledgement has been made whenever the work described is based on the findings of other investigators.

Sarbajit Dutta

Sarbajit Dutta

CERTIFICATE

I hereby certify that the matter embodied in this thesis entitled "**First-principles and Theoretical Analysis of Electronic, Optical and Vibrational Properties in Layered Materials**" has been carried out by Mr. Sarbajit Dutta at the Chemistry and Physics of Materials Unit, Jawaharlal Nehru Centre for Advanced Scientific Research, Bangalore, India under my supervision and that it has not been submitted elsewhere for the award of any degree or diploma.

Prof. Umesh V. Waghmare

(Research Supervisor)

Acknowledgement

At the very outset, I would like to express my deepest gratitude to my research supervisor Prof. Umesh V. Waghmare for his unstinting support, and heartfelt motivation. It has indeed been a memorable and beautiful experience in working with him. He has always been a constant support throughout my course of academic and non-academic journey at JNCASR. His valuable comments and instructions in preparing presentations, seminars, scientific write-ups, and talks have helped me immensely. I am and will be forever indebted to him for everything.

I am very grateful to all the past and present members of Materials Theory Group who have helped me in many ways during my masters. I am thankful to Koyendrila, Arijit, Shashank, Narendra, Raagya, Surabhi, Unnimaya, Bhuvaneshwari, Sakshi, Aparna, Dr. Lakshay, Dr. Prasad, Dr. Arpita Sen, Dr. Arpita Paul, and Dr. Durgesh who have always been helpful to me during my stay at JNCASR.

I am thankful to all my course instructors in and out of JNCASR for their insightful courses which have not only helped me understand the subject to the core but has also opened up new ways many times during my research. I thank Dr. Premkumar Senguttuvan, Prof. Sarit S. Agasti, Prof. Swapan K. Pati, Prof. Eswaramoorthy Muthusamy, Prof. A. Sundaresan, Prof. Meher Prakash, Prof. Ranjan Datta, Prof. Rajesh Ganapathy, Prof. Sridhar Rajaram, Prof. Shobhana Narasimhan, Prof. Umesh V. Waghmare, Prof. N. S. Vidhyadhiraja, Dr. Bivas Saha, Prof. Kanishka Biswas, Prof. Tapas Kumar Maji, Prof. Subir K. Das, Prof. Subhro Bhattacharya (ICTS), and Prof. Arun Mangalam (IIA) for giving their insight in wonderful courses.

I am also thankful to my teachers at St. Xavier's College, Kolkata, especially Prof. Subhankar Ghosh, Prof. Indranath Chaudhuri, Prof. Suparna Roy Chowdhury, Prof. Soma Ghosh, Prof. Tapati Dutta, Prof. Sarbari Guha, Prof. Shibaji Banerjee, Prof. Saunak Palit, Prof. Tanaya Bhattacharyya, Prof. Sudipto Roy, Prof. Gayatri Banerjee, Prof. Aditi Ghosh, Prof. Sanghamitra Das, and Prof. Ananda Dasgupta (IISER Kolkata) for motivating me and inspiring me to take up a career in research in condensed matter physics.

I am thankful to my batchmates Deeksha, Shubhanshi and Sneha who always have been a great support to me. I am also thankful to all my batchmates at St. Xavier's College for helping me out in many ways, and always keeping my spirits high.

I am indeed lucky to have a memorable stay at JNCASR. In fact, my friends in JNCASR have never failed to gift me memorable days which I will cherish forever. I want to thank Deeksha, Deepam, Souradip, Koyendrila, Arijit, Robi, Soumen, Souvik, Dheemahi and Sayan for always boosting up my spirits.

I want to thank the Cultural Committee at JNCASR in which I always been a part of. I would also like to thank Rhythmica Club at IISc for pushing my passion in music to a next level. I would like to thank Ustaad Jainul Abedin, my mentor in music, for always making my days melodious by his indelible tutoring in Hindustani Classical Music.

I am extremely grateful to some of my mentors in school, especially Jayanti ma'am, Anupam sir, Kavita ma'am, Saswati ma'am, Manali ma'am, Sharmistha ma'am for always believing in me. I am thankful to Sudipto sir, Kaushik sir, Amitava sir, Sanjoy sir and Supriyo sir who motivated me in taking up science and pursue a career in physics.

I would also like to thank Chandan and Bindu for their help in all the administrative works. They have really made our stay extremely smooth due to their sheer hard work.

I would like to thank Aruna ma'am, and Kruti for their wonderful hospitality, and making me feel at home.

I would like to acknowledge the Centre for Computational Material Science (CCMS) for providing computational lab courses. I would also like to thank the Comp-lab staff for tending to our problems at any time of the day. I also extend my gratitude to Librarian, Academic and Administrative staff for their efficiency and helpfulness. I thank Dhanvantari staff, Hostel mess, dining hall and utility for food facilities.

Last but not the least, I would like to thank my parents from the very core of my heart. Nothing would have been possible without their love, affection, and selfless support. I thank them for providing me freedom at every stage of life, and always supporting me.

Synopsis

Layered materials refer to materials that are composed of two or more layers stacked on top of each other. These have emerged as an exciting area of research due to their unique properties and potential applications.

Halide perovskite derivatives are a class of layered materials that have drawn a lot of interest recently because of their exceptional optoelectronic characteristics. These substances are made up of layers of metal cations and halide ions stacked in a perovskite fashion. The optical and electrical properties of the material can be adjusted by adding other metals and halides to the structure. As a result, a variety of halide perovskite derivatives have been created and are used in solar cells, light emitting diodes, and other optoelectronic devices.

Another layered substance that has attracted a significant lot of interest recently is bilayer graphene. Bilayer graphene is made up of two layers of graphene that have been placed on top of one another. Graphene is a single layer of carbon atoms organised in a hexagonal lattice. Bilayer graphene has been demonstrated to exhibit a number of intriguing electrical properties as a result of the special electronic characteristics of graphene.
Bilayer graphene has also been employed in a variety of applications, including the creation of quantum devices and high-speed transistors. Bilayer graphene's characteristics can be engineered for unique applications by adjusting the stacking arrangement.

In **chapter 1**, we provide an introduction to the main theme of the thesis. It involves a brief history of the field, followed by a short review of the recent advancements in this field.

In **chapter 2**, we provide the methods and formalism needed for our computational simulations. We provide a basic insight into the density functional theory (DFT), and how it can be implemented in modern day computer simulations.

In **chapter 3**, we focus on the electronic and optical properties of halide perovskite derivatives. Essentially, we focus on $Cs_3Sb_2I_9$ which has immense optoelectronic applications. We employ DFT techniques and GW methods to study the optical absorption spectrum of the material and identify the electronic transitions responsible for such a spectrum.

In **chapter 4**, we investigate sliding in irrational directions in bilayer graphene. We study the electronic and vibrational properties under such sliding. In fact, break in symmetry due to sliding gives rise to novel phenomena in these systems. The electronic band structure and the phonon spectrum do change a lot under such sliding motions.

List of Publications

1. Optical properties of $Cs_3Sb_2I_9$: First-principles analysis
   (in collaboration with the group of Prof. Hiren Ghosh, Institute of Nano Science and Technology (INST), Mohali, Ajit Singh Nagar, Punjab 140306)
   [*Manuscript under preparation*]

2. Investigations in sliding bilayer graphene in irrational directions
   [*Manuscript under preparation*]

List of Figures

List of Tables

Table of Contents

Chapter 1

Introduction

Perhaps, one of the most influential works of Shakespeare involves the transcendental lines in his ‘Seven Ages of Man’. Quite ironically, humankind has seen growth in science and technology following the footsteps of what is referred to as the ‘Seven Ages of Materials’ [1]. Right from the Stone Age in the human prehistory to Bronze, Iron, Aluminium, Glass, Plastic, and finally the Silicon age, shows how intricately understanding materials is related to human civilization, and intellectual growth of humankind.

One can say, however, that the eighth wonder in materials sciences is not a new material, but the advent of computers, and their immense functionality which has brought about quite a revolution in the field of the scientific endeavour to understand and appreciate the rich playground which materials science offers us. As rightly said by Karl Marx, that “social revolution” should draw “its poetry from the future” [2], scientific revolution too should rest its fulcrum over the shoulders of its futuristic imagery. Needless to say, computers have speeded up research in materials science to the future by manifold times.

One of the precursors in this advancement, comes from the great minds of the intellects like Schrodinger, Bohr, Einstein, Feynman, and others, who have shaped for us “A Beautiful Mind”, more formally known as Quantum Mechanics [3]. It shows how a microscopic description of matter can be immensely successful in predicting and understanding matter itself and its properties on a fundamental level. The celebrated equation called the Schrodinger’s equation has proved itself time and again that it does have a herculean power of predicting what happens around us. But like all great things in life, Schrodinger’s equation too has its own

limit. It turns out that solving it for a real system (with Avogadro number of particles) is impractically difficult. This was pointed out with an estimate by physicist Douglas Hartree, who said that to describe an iron atom on a coarse grid one would need to store more numbers than there are particles in the solar system. So, the way out there, is to approximate and simplify our problem.

The nineteenth century saw a great deal of developments in simplifying the so called ‘many body problem’ with approximations and assumptions [4]. The theories given by eminent physicists like Born and Oppenheimer, Hartree and Fock, Thomas and Fermi, and others proved to be quite successful in describing the problem. However, perhaps, the state-of-the-art theory was still yet to be devised, and formulated.

Walter Kohn, a young and enthusiastic jew in the 1950s, was a survivor from the holocaust by Nazi Germany [5]. He soon with his sheer dedication and perseverance was able to lay the foundations of the one of the most successful theories in quantum many body physics, alongside the geniuses of Pierre Hohenberg, and later Lu Jeu Sham. The theory which came to be known as the density functional theory (DFT), started to be used as one of the revolutionary ideas in the field of many body physics. With computers coming into the picture, DFT became even more popular, as now one could run calculations on a computer, which are difficult to solve manually otherwise. Walter Kohn was awarded the prestigious Nobel prize in 1998 in Chemistry "for his development of the density-functional theory".

First principles calculations based on DFT helps us to predict properties of real materials to an extremely good accuracy. Experiments do validate mostly all the results obtained from DFT. It is indeed, a very successful theory to say the least. In fact, it is also one of the cheapest ways of predicting different properties of materials. The essential idea behind first principles calculations, as known as *ab initio* method, is to apply the basic laws and assumptions of many body physics and come up with the structure and properties of materials, without taking inputs from experiments. Both microscopic and macroscopic properties of a typical material, in the bulk form, surfaces and interfaces, can be easily predicted.

Layered materials were perhaps always in use, right from ancient civilizations, but got special attention only very recently. Graphite, an allotrope of carbon, is probably the best-known example among these. It was already used by Neolithic Danubians, in 4000 BC, for paint used in pottery [6]. More recently, research in this field got accelerated increasingly once graphene sheets were exfoliated in 2004 [7]. According to John Dewey, "Every significant breakthrough

in science has issued from a new audacity of the imagination." Graphene's discovery served as a compelling argument. Canadian theorist John Russell Wallace already foresaw the relativistic behaviour of graphene electrons using tight binding models in 1947, though very few believed that such a monolayer could exist. However, in 2004, Andre Geim and Konstantin Novoselov changed the paradigm completely, when they could exfoliate graphene sheets experimentally, leading to the 2010 Nobel prize in Physics [8]. Researchers took interest in layered materials ever since. Among the other layered materials, transition metal dichalcogenides (e.g., MoS_2, $MoSe_2$), certain metal halides (e.g., PbI_2 and $MgBr_2$), and oxides (e.g., MnO_2, MoO_3), perovskites (general form ABO_3), insulating hexagonal boron nitride (h-BN) and layered silicates (clays, micas) are notable mentions.

This new class of materials is essentially interesting due to a broad range of emergent phenomena they exhibit in response to various perturbations. In this thesis, two extremely popular layered materials have been studied — a halide perovskite derivative $Cs_3Sb_2I_9$, which has immense photovoltaic applications, and bilayer graphene which offers a rich playground for major fundamental understanding of condensed matter phases. The properties which have been looked upon are the electronic, optical, and vibrational properties.

Bibliography

[1] https://eandt.theiet.org/content/articles/2019/09/the-seven-ages-of-materials/

[2] Karl Marx, in *The Karl Marx Library*, edited by Saul K. Padover (McGraw Hill, New York, 1972) Vol. 1, p. 245–46.

[3] Nouredine Zettili, *Quantum mechanics: concepts and applications* (John Wiley & Sons, Ltd, New Jersey, 2003).

[4] Peter William Atkins and Julio de Paula, *Atkins' Physical Chemistry* (W. H. Freeman and Company, New York, 2006).

[5] Lu J. Sham, Nature **534**, 7605 (2016).

[6] R. W. Ehrich, *Chronologies in Old World Archaeology* (University of Chicago Press, Chicago 1992).

[7] K. S. Novoselov, A. K. Geim, S. V. Morozov, D. Jiang, Y. Zhang, S. A. Dubonos, I. V. Grigorieva, A. A. Firsov, Science, **306**, 5696 (2004).

[8] https://www.nobelprize.org/prizes/chemistry/1998/summary/

[9] P. Miró, M. Audiffred and T. Heine, Chemical Society Reviews, **43**, 6537 (2014).

Chapter 2

Methods and Formalism

The aim of this chapter is to briefly discuss the theoretical background and the computational methods involved in our first-principles calculations within the framework of density functional theory. The ability of quantum mechanics to predict the total energy of a system of electrons and nuclei has been the driving force to perform quantum-mechanical calculations.

In the first section, we show how any property exhibited by a material can be described by the total quantum mechanical Hamiltonian involving the interaction between the electrons, the ions, and the interactions among themselves. We then describe certain approximations e.g., Born-Oppenheimer and classical nuclei approximations considered while calculating the electronic structure of a material.

The next section involves converting these many body Schrödinger equation to a set of coupled one electron equations using Hohenberg-Kohn theorems and Kohn-Sham Ansatz. The Kohn-Sham method can then be practically used to obtain the total energy of system of electrons and nuclei which is the essential quantity needed to calculate many physical quantities. The first order derivatives of total energy give important physical quantities like polarization, magnetization, and forces while dielectric constant, magnetic susceptibility, force constant can be obtained by taking the second order derivatives of the total energy.

Furthermore, the next section involves discussing the theoretical approaches within the density functional perturbation theory (DFPT) used to describe phonons which are the quanta of lattice vibrations in a given material.

2.1 Grand Hamiltonian

The full Hamiltonian of a material considering all possible interactions between electrons and ions [1] is given in Eq. (2.1) as,

$$H = -\sum_{I}\frac{1}{2M_I}\nabla_{\mathrm{I}}^2 - \frac{1}{2}\sum_{i}\nabla_{\mathrm{i}}^2 + \frac{1}{2}\sum_{I}\sum_{I\neq J}\frac{Z_I Z_J}{|R_I - R_J|} + \frac{1}{2}\sum_{i}\sum_{i\neq j}\frac{1}{|r_i - r_j|} - \sum_{I}\sum_{i}\frac{Z_I}{|R_I - r_i|} \tag{2. 1}$$

Here, electrons are denoted by lowercase subscripts and nuclei by uppercase subscripts. The first term in the above expression is the kinetic energy of nuclei, the second term represents the kinetic energy of electrons, the third and fourth terms represent the interaction between electrons and the interaction between nuclei respectively. Fifth term also termed as external potential denotes interaction between electrons and nuclei. It should also be noted that we have used atomic units, where the charge of an electron, the mass of an electron, reduced Planck's constant, and the electrostatic constant are all taken as unity.

Given this total Hamiltonian of any system, we can write the time-independent Schrödinger equation as,

$$H\psi(\boldsymbol{R_I}, \boldsymbol{r_i}) = E\psi(\boldsymbol{R_I}, \boldsymbol{r_i}) \tag{2. 2}$$

where $\psi(\boldsymbol{R_I}, \boldsymbol{r_i})$ is the total wave function consisting of the electronic and ionic part.

If total energies can be calculated, any physical property that can be related to total energy can be determined computationally. The problem in obtaining exact quantum mechanical total energy is to solve a set of very complicated coupled differential equation. This is because any material has a very large number of ions and electrons with their degrees of freedom coupled to each other. The only possible solution is taking into account reasonably good approximations.

2.2 Adiabatic Born-Oppenheimer Approximation

The adiabatic approximation (Born-Oppenheimer approximation [2]) is one of the most important assumptions made to simplify the grand Hamiltonian of a system of interacting electrons and ions. This assumption is based on the fact that the mass of the nucleus is approximately 1836 times larger than that of an electron hence the time scale associated with the motion of the nuclei (ions) are much slower than that associated with electrons. Therefore, kinetic energy of nuclei can be neglected in comparison to that of electrons. The electrons instantaneously follow the motion of the ions while remaining in the same stationary (adiabatic) state (ground or excited). If this condition is followed, then the dynamics is said to be adiabatic.

If H is the total Hamiltonian of the system, then,

$$H = T_n + U_{nn} + H_e \tag{2. 3}$$

where the electronic Hamiltonian of a system can be written in a short notation as,

$$H_e = T_e + + U_{ee} + V_{ext} \tag{2. 4}$$

where T_e and T_n are the kinetic energies of electrons and nuclei respectively. U_{ee} and U_{nn} are electron-electron and nuclear-nuclear interaction potential respectively. V_{ext} is the interaction potential between the electrons and nuclei.

Though Born-Oppenheimer approximation reduces the difficulty to determine the ground state for a given set of atoms and their positions, quantum mechanical solution of Eq. (2.3) for the large number of atoms is still a challenge. Therefore, determination of the ground state is quite hard and requires additional approximations.

2.3 Classical nuclei approximation

The second most important assumption made in simplifying the electronic structure of a matter is the classical nuclei approximation. Since the nuclear masses are very heavy as compared to electrons, the wave functions for nuclei are much more localized and therefore one can assume that quantum phase coherence of the nuclear wave functions is very less or does not exist at all. This led to the safe assumption of treating nuclei as classical particles. Within this

approximation, the total nuclear wave function can be expressed as the product of all individual nuclear wave function. By doing so we can neglect the exchange and correlation interactions among them. The dynamics of the mean values of position and momentum operators can be obtained through Ehrenfest's theorem.

2.4 Independent electron approximation

Independent electron approximation is the oldest approximation which considers two basic independent-particle approaches that may be classified into "non-interacting" or Hartree method and Hartree-Fock method. In Hartree method, only the classical electrostatic Coulomb interaction energy is considered while neglecting the exchange and correlation effects. Hartree did not consider the asymmetric nature of electronic wavefunctions.

But in Hartree-Fock method, in addition to the electrostatic interaction energy, the exchange effect due to Pauli principle and correlation effect are taken into account. Antisymmetric nature of electrons was considered in the Hartree-Fock Approximation. In this framework, asymmetric electronic wavefunction can be written in the form of a Slater determinant such that the wavefunctions are indistinguishable.

In modern DFT, the electronic Hamiltonian is taken to be non-interacting like in Hartree approach and electrons are assumed to move in an effective external potential chosen so as to incorporate the exchange-correlation effect approximately.

2.5 Hohenberg-Kohn theorems

The framework of DFT is based on two theorems called Hohenberg-Kohn theorems [3]:

Theorem I: The external potential $V_{ext}\ (\boldsymbol{r})$ of any system of interacting particles can be determined uniquely by the ground state particle density $n_0(\boldsymbol{r})$ within an additive constant.

Theorem II: For any given external potential $V_{ext}\ (\boldsymbol{r})$, the universal functional for energy E[n] of the system can be defined in terms of particle density $n(\boldsymbol{r})$. The exact ground state energy of the system is the global minimum value of this functional, and the density $n(\boldsymbol{r})$ that minimizes this functional is the exact ground state particle density $n_0(\boldsymbol{r})$.

Based on these two theorems, the 3Ne (Ne is number of electrons) variables in the problem are reduced to a problem involving function of only three variables of $n(\boldsymbol{r})$, and the total energy functional can be written:

$$E_{HK}[n] = F_{HK}[n] + \int d^3r \; V_{ext}\,(\boldsymbol{r})\, n(\boldsymbol{r}) + E_{nn} \tag{2. 5}$$

$$F_{HK}[n] = T[n] + E_{int}[n] \tag{2. 6}$$

Here, $F_{HK}[n]$ is the includes kinetic energy $T[n]$ and potential energy $E_{int}[n]$ of the interacting particles electrons, and E_{nn} is the nuclei-nuclei Coulomb interaction in the system.

Though these two theorems prove existence of a universal functional $F_{HK}[n]$ (only a functional of density $n(\boldsymbol{r})$), they do not provide a practical scheme for determining the ground state density $n_0(\boldsymbol{r})$. In 1965, Kohn and Sham proposed an ansatz for the ground state density $n_0(\boldsymbol{r})$ to simplify the problem.

2.6 Kohn-Sham Ansatz

Kohn-Sham ansatz [4] is a mathematical assumption that replaces the ground state density of an original interacting many-body system by a system of auxiliary noninteracting particles. Thus, calculations of an original system can be performed on an auxiliary non-interacting particles system with the total energy functional given by,

$$E_{KS}[n] = T_s[n] + \int d^3r \; V_{ext}\,(\boldsymbol{r})\, n(\boldsymbol{r}) + E_H[n] + E_{XC}[n] + E_{nn} \tag{2. 7}$$

Here, $n(\boldsymbol{r})$ is charge density of auxiliary system determined by the sum of square of N_e non-interacting electrons wave functions $\psi_i(\boldsymbol{r})$

$$n(\boldsymbol{r}) = \sum_{i=1}^{N_e} |\psi_i(\boldsymbol{r})|^2 \text{ and } N_e = \int d\boldsymbol{r} \; n(\boldsymbol{r}) \tag{2. 8}$$

Furthermore, $T_s[n]$ is the kinetic energy of the non-interacting electrons, and is given by,

$$T_s[n] = -\frac{1}{2}\sum_{i=1}^{N_e} < \psi_i(\boldsymbol{r}) \mid \nabla^2 \mid \psi_i(\boldsymbol{r}) >$$

(2. 9)

Also, $E_H[n]$ is the Hartree energy, classical interaction energy of the electron density interacting with itself, and defined as,

$$E_H[n] = \frac{1}{2}\int \frac{n(\boldsymbol{r})\, n(\boldsymbol{r}')}{|\, \boldsymbol{r} - \boldsymbol{r}'|}\, d\boldsymbol{r}\, d\boldsymbol{r}'$$

(2. 10)

Again, $E_{XC}[n]$ is the exchange-correlation energy of electrons that takes into account all the quantum mechanical effects of

(i) difference in kinetic energy of the many body interacting system and set of non-interacting system, and

(ii) residual energy contributions due to the exchange asymmetry of electrons and their spatial correlations.

Thus, $E_{XC}[n]$ is given by,

$$E_{XC}[n] = \ (T[n] - T_s[n]) + (E_{int}[n] - E_H[n])$$

(2. 11)

The exact form of $E_{XC}[n]$ is unknown and will be discussed shortly. In this approach, the Hamiltonian of an auxiliary non-interacting particles is called Kohn-Sham Hamiltonian (H_{KS}), and written as,

$$H_{KS} = -\frac{1}{2}\sum_i \nabla_{\mathrm{i}}^2 + V_{KS}(\boldsymbol{r})$$

(2. 12)

Here, the Kohn Sham potential $V_{KS}(\boldsymbol{r})$ is expressed as the sum of the external potential $V_{ext}(\boldsymbol{r})$, Hartree potential $V_H(\boldsymbol{r})$, and the exchange correlation potential $V_{XC}(\boldsymbol{r})$.

$$V_{KS}(\boldsymbol{r}) = V_{ext}(\boldsymbol{r}) + V_H(\boldsymbol{r}) + V_{XC}(\boldsymbol{r})$$

(2. 13)

The exchange correlation potential can be obtained from the exchange correlation energy as:

$$V_{ext}(\boldsymbol{r}) = \frac{\partial E_{XC}[n]}{\partial n(\boldsymbol{r})}$$

(2. 14)

The Hartree term describes the electronic charge distribution of the electrons.

$$V_H = \frac{1}{2}\int \frac{n(\boldsymbol{r}')}{|\,\boldsymbol{r}-\boldsymbol{r}'|}\,d\boldsymbol{r}'$$

(2. 15)

Now, the single particle Kohn-Sham equations are:

$$\left(-\frac{1}{2}\sum_i \nabla_i^2 + V_{KS}(\boldsymbol{r})\right)\psi_i(\boldsymbol{r}) = \varepsilon_i\,\psi_i(\boldsymbol{r})$$

(2. 16)

or $\quad H_{KS}\,\psi_i(\boldsymbol{r}) = \varepsilon_i\,\psi_i(\boldsymbol{r})$

(2. 17)

Since Kohn-Sham equations are non-linear equations (Eq. 2.16), a self-consistent iterative method is used to solve them as illustrated in figure 2.1.

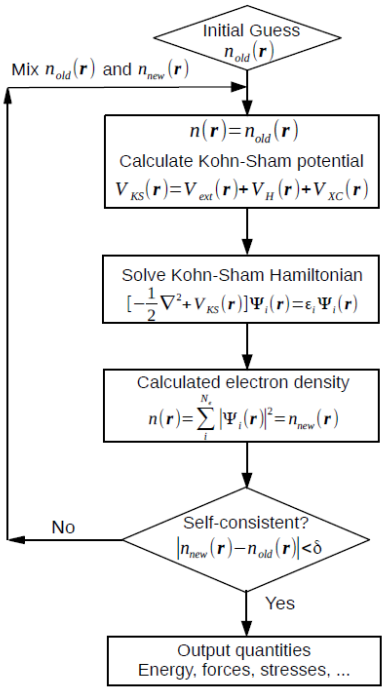

Figure 2.1 *Flow chart showing the self-consistency loop for the iterative solution of Kohn-Sham equations.*

2.7 Approximations to the Exchange-Correlation Functional

As mentioned earlier, the exact form of $E_{XC}[n]$ is unknown, and it requires further approximations. Towards this, many approximations have been proposed, and among all available approximations, local density approximation (LDA) [5-8] and generalized gradient approximation (GGA) [9] are the most commonly and widely used schemes to estimate the exchange-correlation energy.

2.7.1 Local Density Approximation (LDA)

In LDA, the effect of exchange and correlation are considered to be local in nature as it was assumed by Kohn & Sham [4]. In this approach, the inhomogeneous system is thought to be locally homogeneous. The exchange-correlation energy can be obtained by integrating the exchange-correlation energy density at each point over whole space. The LDA approximation proves to be very successful for many systems especially for those whose electron density is quite uniform such as bulk metals, ionic crystals etc. LDA fails to produce some properties (e.g., band gap) in semiconductors, strongly correlated systems due to fact that the excitation spectrum of homogeneous electron gas is gap-less, and exchange-correlation energy is regular. Another failure is its ability to capture weak inter-molecular bonds, hydrogen bonds etc.

The exchange-correlation energy in LDA is thus given by,

$$E_{XC}^{LDA}[n] = \int d^3\boldsymbol{r}\, n(\boldsymbol{r})\varepsilon_{XC}[n(\boldsymbol{r})] \tag{2. 18}$$

In LDA several aspects like inhomogeneity of electrons, non-local exchange correlation effect, complete cancellation of self-energies of electrons etc were not present.

The parametrizations by Perdew-Zunger (PZ), Perdew-Wang (PW), and Vosko-Wilk-Nusair (VWN) in the exchange correlation functional are the LDA functionals used commonly in DFT calculations [5-8].

2.7.2 Generalized Gradient Approximation (GGA)

The improvement of LDA resulted in the development of GGA. In general, the exchange-correlation energy in GGA can be written as,

$$E_{XC}^{GGA}[n] = \int d^3\boldsymbol{r}\, n(\boldsymbol{r})\varepsilon_{XC}[n(\boldsymbol{r}), \nabla n] \tag{2. 19}$$

Here, the exchange-correlation energy is expressed as a sum of contributions from each point in real-space depending only on the density and its gradient at each point and independent of other points. The GGA method turns out to be better than LDA in the sense that it improves binding energies, bond lengths. GGA also improves the band gap of semiconductors over LDA. Semiconductors are also better described in GGA than LDA.

Perdew and Wang (PW91) and Perdew, Burke and Ernzerhof (PBE) are some of the parametrizations of the GGA functional [9].

2.8 Pseudopotentials

Based on the nature of chemical activity of electrons in a material, they can be divided into two types, (i) core electrons, and (ii) valence electrons. In solids or molecules, the core electrons are tightly bound to the nucleus and hence are not involved in bonding. The core electrons are relatively unaffected by the chemical environment of an atom. The contribution of core electrons to the total binding energy remains unaffected when isolated atoms are brought together to form a molecule or a crystal. The actual energy differences of interest involve changes in the valence electron interaction and energies. The contribution of valence electrons to the total binding energy is a much larger fraction than that of valence electrons and makes it easier to calculate accurately. The reason is the difficulty in numerical representation of highly localized core electron wave functions because of strong nuclear Coulomb potential. So, core electrons are removed from the calculation, and the interaction of the valence electrons with the nucleus plus the core states is replaced by an effective screened potential.

Pseudopotential approximation [10] takes this into account and removes core electrons by replacing their effects and strong ionic potential by a weak and smooth pseudopotential that act on a group of pseudo wavefunctions of valence electrons.

Pseudopotentials are constructed using a cut off radius (r_c) which sort of separates out the valence region from the core region. The region beyond r_c is treated as a valence region and within r_c as the core region. The value of r_c is chosen in such a way that the last node of the all electron wavefunction fall inside it. Pseudopotential and all electron wavefunction are identical outside the cut off radius. Traditionally, a pseudopotential is divided into local and non-local parts, where the former is long-ranged, and the latter is typically short-ranged.

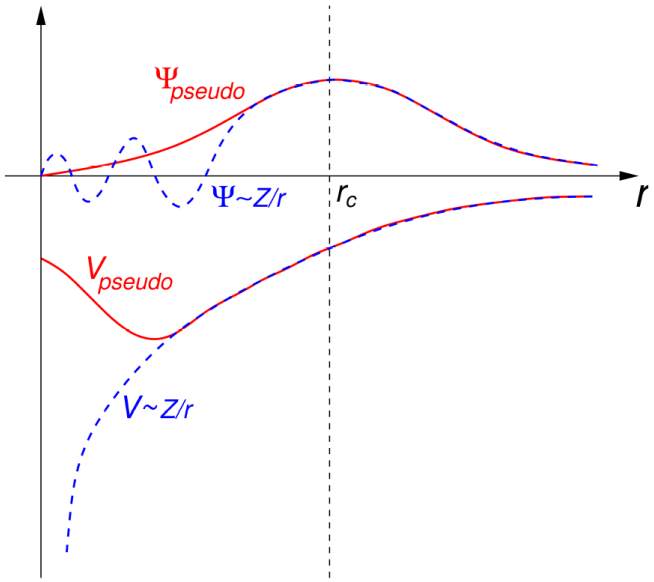

Figure 2.2 *Schematic representation of all-electron (dashed lines) and pseudo electron (solid lines) potentials and their corresponding wavefunctions. The radius at which all electron and pseudo electron value matches is designated r_c. This figure is taken from https://en.wikipedia.org/wiki/Pseudopotential.*

2.9 Basis Sets

In order to numerically solve the Kohn Sham equations, one requires to choose a mathematical representation for the one electron orbital. The requirement is a basis to expand the wave functions and then truncating the basis such that the calculation time remains finite. Different classification of basis sets includes plane-waves [11], atomic orbitals [12, 13], and their combination (mixed basis) [14]. The atomic orbital basis is the most commonly used basis set for isolated systems such as atoms and molecules. A basis set of mutually orthonormal plane waves is used for representation of extended periodic systems.

Plane-wave basis set is widely used in the simulations of materials that have periodicity at least in one dimension. Typically, one should have as many number of plane waves as possible to get most accurate results (in principle, infinity).

The potential experienced by an electron is a periodic one in solids, and is invariant under crystal lattice translation i.e., $V_{ext}(\boldsymbol{r}) = V_{ext}\ (\boldsymbol{r} + \boldsymbol{R})$ where, $\boldsymbol{R}$ is a lattice vector. Bloch's theorem states that in periodic solid each electronic wave functions can be written as,

$$\psi_{nk} = u_{nk}(\boldsymbol{r})e^{i\boldsymbol{k}.\boldsymbol{r}} \tag{2. 20}$$

Here, $u_{nk}(\boldsymbol{r})$ is a periodic function which can be further expanded in terms of plane waves following Fourier theorem.

$$u_{nk} = \frac{1}{\sqrt{V}} \sum_{G} C_{nk}\ (\boldsymbol{G})\ e^{i\boldsymbol{k}.\boldsymbol{G}} \tag{2. 21}$$

Therefore, the electronic wave functions can be written as a sum of plane waves.

$$\psi_{nk} = \frac{1}{\sqrt{V}} \sum_{G} C_{n,k+G}\ (\boldsymbol{G})\ e^{i(\boldsymbol{k}+\boldsymbol{G}).\boldsymbol{r}} \tag{2. 22}$$

Where $\boldsymbol{G}$ and $\boldsymbol{k}$ are reciprocal lattice vector and Bloch wave-vector in the Brillouin zone, respectively, and $C_{n,k+G}$ is an expansion coefficient. In practice the sum is truncated by introducing a kinetic energy cut-off (E_{cut}) which determines the number of plane-waves satisfying the following condition:

$$\frac{\hbar^2 k^2}{2m_e} \mid \boldsymbol{k} + \boldsymbol{G}|^2 \ \leq E_{cut} \tag{2. 23}$$

The cut-off energy (E_{cut}) is increased until the energy differences converge to a desired accuracy.

2.10 Phonons

Phonon is a quasiparticle and quantum of vibrational energy associated with collective motion of atoms in materials. The concept of phonons provides a powerful tool to study the properties of materials which are governed by atomic displacements.

Phonon-dispersion which is the behaviour of vibrational frequency (ω) versus wave-vector (q), reveals interesting physics of materials that governs stability of structures, thermodynamic properties, and structural phase transformation of crystalline materials.

2.10.1 Linear response

DFT linear-response (DFT-LR) [15] is an approach to computing the second derivative of the total energy with respect to a given perturbation. Since the force constant matrix is a second derivative of ground state energy with respect to atomic displacements (u), the linear response provides a powerful mechanism to calculate phonons at an arbitrary wave-vector (q). This method is efficient and hence widely used in first-principles calculations, and also known as density functional perturbation theory (DFPT). In this approach, the force constant matrix ($K_{i\alpha,j\beta}$)

$$K_{i\alpha,j\beta} = \frac{\partial^2 E}{\partial u_{i\alpha}\partial u_{j\beta}} = \frac{\partial^2 E_{ion-ion}}{\partial u_{i\alpha}\partial u_{j\beta}} + \int n(\boldsymbol{r})\frac{\partial^2 V_{ext}}{\partial u_{i\alpha}\partial u_{j\beta}}\, d\boldsymbol{r} + \int \frac{\partial n(\boldsymbol{r})}{\partial u_{i\alpha}}\frac{\partial^2 V_{ext}}{\partial u_{j\beta}}\, d\boldsymbol{r} \quad (2.\ 24)$$

It is clear from Eq. (2.24) that $K_{i\alpha,j\beta}$ depends on the ground state charge density ($n(\boldsymbol{r})$) and its first derivative (linear-response) with respect to atomic displacement $\frac{\partial n(\boldsymbol{r})}{\partial u_{i\alpha}}$.

To calculate $K_{i\alpha,j\beta}$ Eq. (2.24) is evaluated within the framework of first-principles calculations by solving first-order Kohn-Sham equations.

2.11 GW Method

It is evident that a popular technique for predicting the ground state properties of materials, such as energy, lattice parameters, force, mechanical strength, vibrations, etc., is density functional theory (DFT). Yet, it is not very successful in identifying the many-body system's excited state features, such as the bandgap, optical spectra, and excitons. Consequently, it is

necessary to move beyond the single particle framework in order to explain the system's excited state features. Going from a single particle to Landau's quasi-particle (QP) energies [16] is essential since the latter may be measured through experiments. These experiments mainly involve photoemission and inverse photoemission spectroscopy techniques, which adds and subtracts electrons from the system. Similar to this, single particle calculations are used to determine QP energies. The many body perturbation theory (MBPT) uses Green's function methods [17]. It describes how an electron's addition or removal spreads throughout the system. Similar to how difficult it is to solve the exchange-correlation term in DFT, self-energy is the most challenging term in this context. Self-energy is an abstract, energy-dependent concept. The lifetime of the particle and the propagation of the electron or hole from one point to another within the system are described, respectively, by the real and imaginary parts of self-energy.

In the GW approximation the electrons are not considered to be independent particles, instead an electron that moves through a material interacts with the other electrons and polarizes its surroundings. The electrons are said to be dressed by this polarization cloud they induce in their immediate environment. These dressed electrons are called quasiparticles.

These quasiparticles (eigenstates and eigen energies) are obtained by solving the following one-electron equation:

$$(T + V_{ext} + V_H)\psi_{nk} + \int d\boldsymbol{r}\, \Sigma(\boldsymbol{r}, \boldsymbol{r}', E_{nk})\psi_{nk}(\boldsymbol{r}') = E_{nk}\psi_{nk}(\boldsymbol{r}) \tag{2. 25}$$

In the QP equation, the self-energy term $\Sigma(\boldsymbol{r}, \boldsymbol{r}', E_{nk})$ is mentioned explicitly. The eigenstates and eigenvalues of the single-particle excitations must be ascertained in order to solve the eigen value problem that results from the solution of the quasi-particle equation. Self-energy computation is an extremely difficult task. This technique, sometimes known as the GW approach, was first put forth by Hedin in 1965 [17-19].

In GW the self-energy Σ, is approximated as $\Sigma = GW$, the product of a Green's function G and the screened Coulomb interaction W, hence the name. The dielectric screening of the Coulomb interaction is commonly calculated within the random-phase approximation (RPA): in this approximation the electronic interactions between an electron that travels through a medium and its environment are strictly limited to polarization events.

DFT orbitals serve as the starting point for GW computations. Initial G and W are subsequently built. Depending on how G and W are updated, GW methodology can take many distinct forms. The most popular and straightforward technique is single shot GW (G_0W_0). For this kind of calculation, a relevant starting point is crucial. Hence, the initial starting point, or DFT orbitals, is crucial for a single shot GW. Bandgap is mostly delivered via the single shot GW method in accordance with experimental data.

However, GW has several real-world drawbacks, such as high computational cost and enormous memory storage requirements. This is because there must be a big number of free bands, as well as a large number of basis functions N. The electronic polarizability and the correlation portion of the self-energy operator must converge before the former can be used. In theory, it requires an infinite number of bands, making it virtually impossible. The accurate prediction of the self-energy and the optical response function depends on the convergence of the number of unoccupied bands and the basis function N. Hence, one must carefully take sufficient number of bands so that convergence is achieved.

Bibliography

[1] R. M. Martin, *Electronic structure: basic theory and practical methods* (Cambridge university press, Cambridge, UK, 2004).

[2] M. Born and R. Oppenheimer, Annalen der physik **389**, 457 (1927).

[3] P. Hohenberg and W. Kohn, Phys. Rev. **136**, 864 (1964).

[4] W. Kohn and L. J. Sham, Phys. Rev. A. **140**, 1133 (1965).

[5] R. O. Jones and O. Gunnarsson, Reviews of Modern Physics **61**, 689 (1989).

[6] D. M. Ceperley and B. Alder, Physical Review Letters **45**, 566 (1980).

[7] S. H. Vosko, L. Wilk, and M. Nusair, Canadian Journal of physics **58**, 1200 (1980).

[8] J. P. Perdew and Alex Zunger, Phys. Rev. B. **23**, 5048 (1981).

[9] J. P. Perdew, K. Burke, and M. Ernzerhof, Phys. Rev. Lett. **77**, 3865 (1996).

[10] W. E. Pickett, Computer Physics Reports **9**, 115 (1989).

[11] X. Gonze et al., Computational Materials Science **25**, 478 (2002).

[12] P. O. Widmark, P. A. Malmqvist, and B. O. Roos, Theoretica chimica acta **77**, 291 (1990).

[13] P. O. Widmark, B. J. Persson, and B. O. Roos, Theoretica chimica acta **79**, 419 (1991).

[14] S. G. Louie, K.-M. Ho, and M. L. Cohen, Phys. Rev. B. **19**, 1774 (1979).

[15] S. Baroni, P. Giannozzi, and A. Testa, Phys. Rev. Lett. **58**, 1861 (1987).

[16] LD Landau, Sov. Phys. JETP. **3**, 920 (1957).

[17] Lars Hedin, Phys. Rev. **139**, A796 (1965).

[18] Lars Hedin, J. Phys.: Condens. Matter. **11**, R489 (1999).

[19] F. Aryasetiawan and O. Gunnarsson, Rep. Prog. Phys. **61**, 237 (1

Chapter 3

Optical Properties of $Cs_3Sb_2I_9$: First-principles Analysis*

3.1 Introduction

The energy crisis is a major threat to the sustainable development of our planet. The predominant source of energy being fossil fuels has resulted in a considerable amount of greenhouse gas production, which is a key cause of climate change and global warming. Moreover, there is a serious concern regarding the limited availability of fossil fuels implying that soon they will eventually run out. This could lead to economic instability and geopolitical tensions as countries compete for the remaining resources.

Due to these consequences, environmentally friendly and sustainable energy sources are now required. These sources must not harm the environment. Renewable energy sources including sun, wind, hydro, geothermal, biomass, and others are plentiful, unrestricted, and free of hazardous emissions or pollutants.

One of the most promising renewable energy sources is solar energy. It is copious and unrestricted. It is interesting to note that some materials can be used to harvest it. Such materials usually go by the name of photocatalytic or photovoltaic materials. Light energy is converted into electrical energy by photovoltaic materials and chemical energy by photocatalytic materials.

---

*In collaboration with the group of Prof. Hiren Ghosh, Institute of Nano Science and Technology (INST), Mohali, Ajit Singh Nagar, Punjab 140306.

These materials provide a flexible option for energy production since they may be incorporated into a wide range of applications, such as building materials, transportation systems, and electrical gadgets.

Photovoltaic and photocatalytic materials are mainly semiconductors, whose band gaps are in the visible light range. Both photocatalyst and photovoltaic methods utilize the bandgap difference of the semiconductors. Albeit both show a huge difference in terms of mechanism, conversion, and end product.

In the recent years, hybrid organic-inorganic lead halide perovskites have been widely used in optoelectronic applications, such as photodetectors and light-emitting diodes [1-3]. Recent investigations on the use of lead halide perovskites for photocatalytic purposes, such as the degradation of organic dyes, the reduction of CO2, and the production of hydrogen, have been published [4-9]. This is essentially due to the novel optoelectronic properties of these materials.

Among such materials, methylammonium lead iodide ($CH_3NH_3PbI_3$) has emerged as a remarkable photovoltaic absorber material in recent years [10-12]. However, the main concern in these materials is the presence of lead, which is toxic. Moreover, they are unstable under ambient moist air. Therefore, the quest for a lead-free material having photovoltaic, and photocatalytic applications is quite impeccable.

Halide perovskite derivatives like $Cs_3Sb_2I_9$ fill up the void here [13-14] . These materials are lead-free, hence nontoxic, and have the band gap (typically around 2.05 eV) lying in the visible region. Very recently, some works have experimentally synthesized this material, and have found the desired results. In fact, it has been well reported that the optical absorption of $Cs_3Sb_2I_9$ is comparable to that of $CH_3NH_3PbI_3$. Thus, $Cs_3Sb_2I_9$ is an ideal candidate to replace the lead-based photo devices, due to its superior properties.

$Cs_3Sb_2I_9$ has two polymorphic structures — 2 D layered form (space group $P\bar{3}m1$, no. 164) and a 0 D dimer form (space group *P63/mmc*, no. 194) [13]. In this chapter, we explore the 2D layered structure of $Cs_3Sb_2I_9$ as a potential candidate for optoelectronic applications from first principles density functional theory calculations. This work has been done in collaboration with the group of Professor Hiren Ghosh*, who performed the experiments and measured the optical absorption spectrum of the material.

3.2 Computational Details

The plane wave basis implementation of the quantum mechanical density functional theory (DFT) was used in our calculations, as provided by the Vienna Ab initio Simulation Package (VASP) [15-17]. A generalized gradient approximation (GGA) as parameterized by Perdew-Burke-Ernzerhof (PBE) [18-19] was used to treat the exchange correlation energy functional in DFT. At the same time, PBEsol [20-21] another version of the PBE parameterization was used to study its effect on the crystal structure, and other physical properties of $Cs_3Sb_2I_9$. To represent the interaction between ionic cores and valence electrons, a projector-augmented waves (PAW) pseudopotential [22] was used.

In implementation of VASP, the cut-off energy to represent the electronic wave functions was taken to be 500 eV. Brillouin zone integrations were sampled on Γ -centered uniform mesh of 4x4x3 k-points in our calculations. Electronic occupation numbers were smeared using Gaussian smearing with a broadening of 0.04 eV. Kohn Sham (KS) equations were solved iteratively till the total energy was converged within 10^{-8} eV/cell. Structural relaxation was performed till the Feynman-Hellman forces on each atom were less than 10^{-3} eV/Å and each component of the stress tensor was less than 10^{-2} GPa.

Optical properties of $Cs_3Sb_2I_9$ were further calculated by using the PBE and PBEsol functionals. Norm conserving pseudopotentials were used for such calculations, followed by non-self-consistent calculations over a 12x12x8 k mesh to carry out the Brillouin zone integration. Optical absorbance (in arbitrary units) was calculated from the following relation:

$$\alpha(\omega) = \frac{\sqrt{2}\cdot\omega}{c}\left(\sqrt{(\varepsilon_1^2+\varepsilon_2^2)}-\varepsilon_1\right)^{\frac{1}{2}} \quad (3.1)$$

In equation (1), $\alpha(\omega)$, ε_1 and ε_2 are frequency dependent absorption coefficient, real and imaginary parts of dielectric constant, respectively.

Accurate band structures were obtained from hybrid functional calculations, as standard GGA underestimates the band gap of $Cs_3Sb_2I_9$. In our calculations, HSE06 [23], and HSEsol [24] hybrid functionals were used. These functionals mix a fraction of non-local Hartree Fock exchange with PBE (for HSE06) and PBEsol (for HSEsol), where, in both cases, the mixture fraction α was taken to be 0.25, in addition to the implementation of the screened parameter ω = 0.2 $Å^{-1}$.

To have a more accurate understanding of the optical properties of $Cs_3Sb_2I_9$, excited state method-based calculations like the many body perturbation theory within the framework of single shot GW calculations (G_0W_0) [25-26], which incorporate the random phase approximation (RPA) were performed. The GW method is proved to be more accurate and involves the screened Coulombic interaction and improves the Hartree Fock approximation The PBE functional was considered to be the starting point in such a case. We have considered a sufficient number of unoccupied bands, i.e., a total of 560 bands which is quite larger than the number of occupied orbitals, in our calculations.

We have used post-processing tool VASPKIT [27] to obtain (a) electronic energy structure, (b) orbital projected density of states, (c) transition dipole moment (TDM) between states from valence bands to conduction bands, and (d) visualization of electronic wavefunction at valence band maximum (VBM) and conduction band minimum (CBM). We have used VESTA package to visualize structure.

3.3 Results and Discussions

3.3.1 Crystal Structure

The crystal structure of $Cs_3Sb_2I_9$, as shown in figure 3.1 (a), is found to be trigonal with space group $P\bar{3}m1$ (number 164) under ambient conditions. It should be noted that $Cs_3Sb_2I_9$ is essentially a halide perovskite derivative, which exists in a layered structural form.

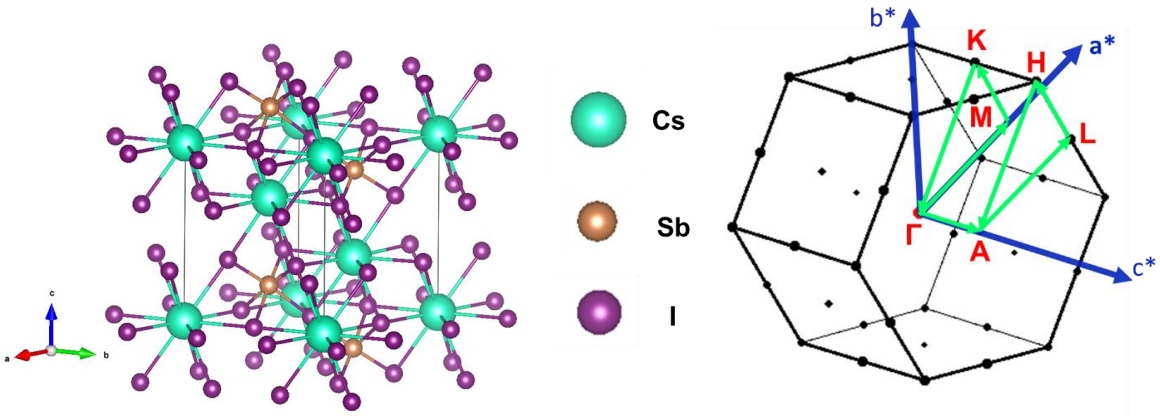

(a) (b)

Figure 3.1 *(a) Crystal structure of $Cs_3Sb_2I_9$ crystallizing in a trigonal structure under ambient conditions, having a space group $P\bar{3}m1$ (number 164). (b) The Brillouin Zone of $Cs_3Sb_2I_9$, showing the high symmetry k points and the path along such a high symmetry direction.*

It is well known from previous studies [13] that local density approximation (LDA) cannot reproduce the lattice parameters to an accurate level. Therefore, the Generalized Gradient Approximation (GGA) has been used to see how well the lattice parameters are reproduced in the geometrically relaxed structure. In fact, two versions of GGA, namely PBE and PBEsol have been used and the lattice parameters obtained have been given in Table 3.1.

Table 3.1 *Comparison of lattice parameters from present calculations, and prior theoretical and experimental values in literature.*

Calculation Method	**Lattice parameter a (Å)**			**Lattice parameter c (Å)**		
	Present	**Theory**	**Experiment**	**Present**	**Theory**	**Experiment**
PBE (GGA)	8.68	8.661[13] 8.664[14]	8.420[28]	10.60	10.625[13] 10.633[14]	10.386[28]
PBEsol	8.34	–		10.29	–	

It is interesting to note that PBEsol captures the lattice parameters of the crystal structure with much higher accuracy. The previous theoretical studies complement our results based on PBE, indicating that the present theoretical level is credible. Prior to this work, PBEsol has not been tested for this materials. However, studies [29] have been performed on similar materials like hybrid halide perovskites where PBEsol have been shown to reproduce the lattice parameters

quite accurately. Even in such studies, PBEsol very slightly underestimates the lattice parameters with respect to experiments, very similar to our present calculations, and unlike PBE functional, which slightly overestimates the lattice parameters. Indeed, one can see that the accuracy level of PBEsol in reproducing the lattice parameters is significantly higher than its PBE counterpart.

3.3.2 Electronic Properties

The calculated band structure of $Cs_3Sb_2I_9$ along the high symmetry k-points in the Brillouin zone is shown in figure 3.1 (b). Both PBE, and PBEsol versions of the GGA reproduce the band structure qualitatively. It is a well-known problem that GGA underestimates the bandgap of a given material. In order to overcome this problem, we have performed hybrid functional calculations with HSE06 and HSEsol hybrid functionals, where the DFT functional part in the hybrid functional was taken from both PBE and PBEsol functionals respectively, mixed with Hartree-Fock exchange. The HSE06 calculations were performed on PBE geometry, and the HSEsol calculations were performed on PBEsol geometry, where both the geometries are the fully relaxed structures.

Quite interestingly, PBEsol, which captures the lattice parameters quite accurately, but fails to reproduce the band structure to a quantitative accuracy, than the PBE functional. The PBE functional emerges to be a better candidate for analysing the band structure of this material. In fact, when the HSE06 hybrid functional is used, the one made using a mixture of PBE and Hartree Fock exchange, gives a very accurate estimate of the band gap, in comparison to the HSEsol hybrid functional which is made using PBEsol and Hartree Fock exchange.

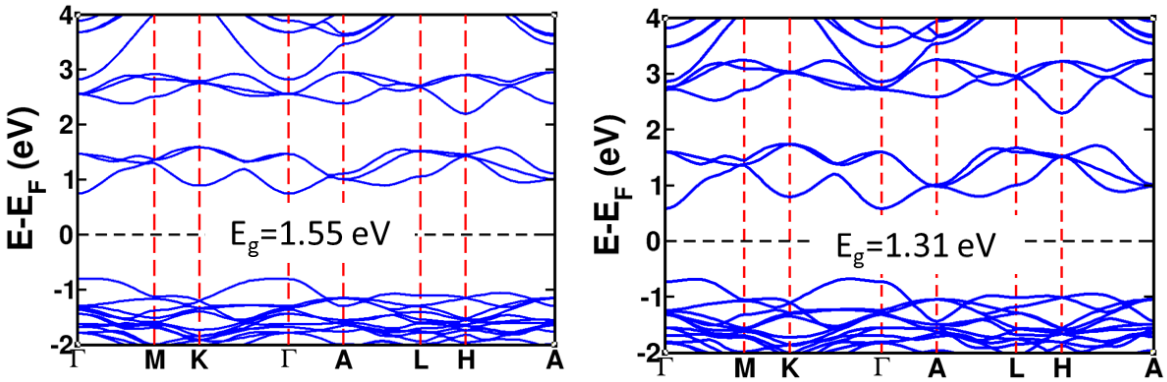

(a) (b)

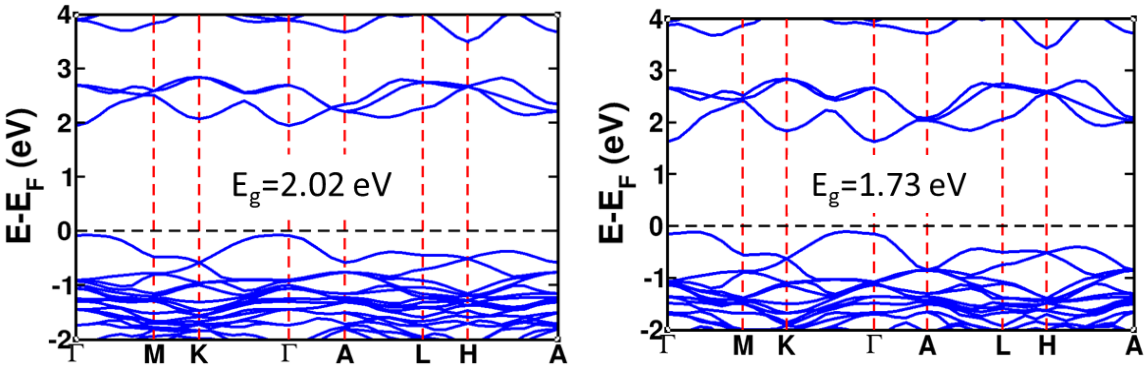

(c) (d)

Figure 3.2 *Band structures of $Cs_3Sb_2I_9$ along high symmetry paths using (a) PBE functional, (b) PBEsol functional, (c) HSE-PBE functional, and (d) HSE-PBEsol functional.*

The estimate of band gap with HSE06 is 2.02 eV which is in good agreement with experimental results suggesting 2.05 eV, and prior theoretical calculations suggesting 2.04-2.06 eV. The results have been summarized in Table 3.2.

Table 3.2 *Comparison of the band gap value from present calculations and prior theoretical and experimental data in the literature.*

Calculation Method	**Present Work: Band gap (eV)**	**Theory: Band gap (eV)**	**Experiment: Band gap (eV)**
PBE	1.55	–	2.05[28]
PBEsol	1.31	–	
HSE06	2.02	2.06[13] 2.04[14]	
HSEsol	1.73	–	

Furthermore, the orbital projected density of states of $Cs_3Sb_2I_9$ shows the various contributions of different orbitals in giving rise to different bands in the band structure.

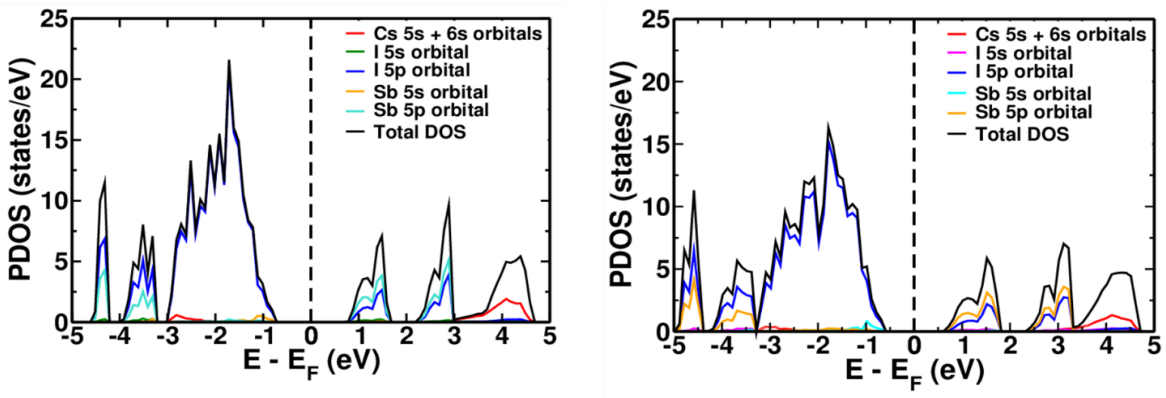

(a) (b)

Figure 3.3 *Orbital projected density of states (PDOS) with (a) PBE functional, and (b) PBEsol functional.*

It is clear from the band structure as shown in figure 3.2 (a)-(d), that $Cs_3Sb_2I_9$ has a direct band gap, as the valence band maxima (VBM) and the conduction band minima (CBM) occur at the same point *(Γ)*. The orbital projected density of states, as in figure 3.3, shows that the VBM is dominated mainly by I 5p orbitals, and the CBM is dominated by I 5p and Sb 5s orbitals. This is further verified by the visualization of the electronic wavefunctions at the VBM and CBM corresponding to the *Γ* point, as shown in figure 3.4.

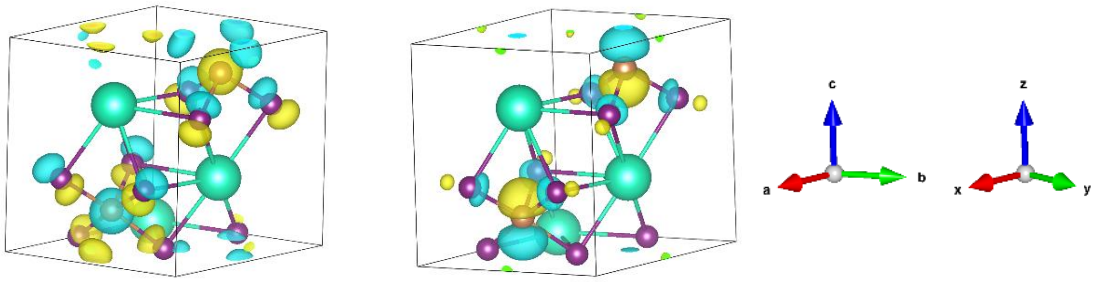

(a) (b)

Figure 3.4 *Isosurfaces of wavefunctions of the states at (a) valence band maximum (VBM), and (b) conduction band minimum (CBM) at Γ point.*

3.3.3 Optical Properties

The optical absorption spectrum has been calculated for $Cs_3Sb_2I_9$. Both PBE and PBEsol functionals have been used in the calculation of the absorption coefficient of $Cs_3Sb_2I_9$. All results have been shown in figure 3.5.

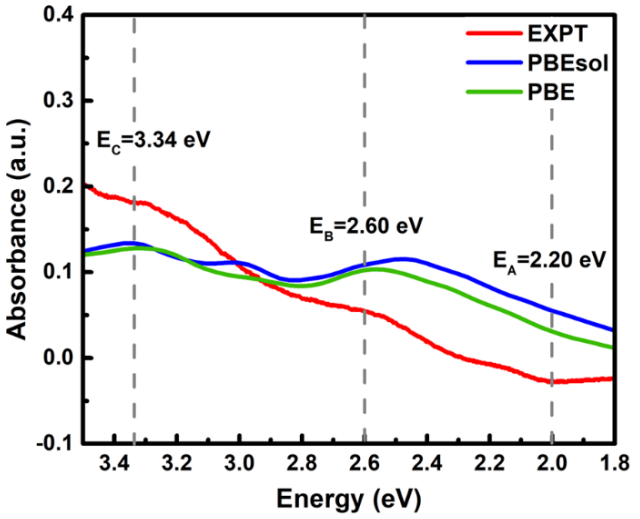

Figure 3.5 *Theoretically calculated optical absorption spectra using PBE and PBEsol functionals.*

It can be seen that PBE functional matches the experimental absorption spectra (as measured by the group of Professor Hiren Ghosh) to a slight better accuracy than PBEsol functional. The peaks in the absorption spectra correspond to several optical transitions from VBM to CBM. The peaks marked in figure 3.5 (dashed lines) are the experimental peaks denoted as E_A, E_B, and E_C. As a matter of fact, no prior study has shed light on the details of the electronic transitions giving rise to such distinct peaks in the absorption spectra. In order to identify such transitions, we have calculated the electron band-wise transition dipole moment (TDM) between different bands along the high symmetry paths in the Brillouin zone, which essentially gives an understanding of the probabilities of transitions from different valence bands to conduction bands, as shown in figure 3.6 (b), and marked the different optical transitions in the band structure of $Cs_3Sb_2I_9$, as shown in figure 3.6 (a).

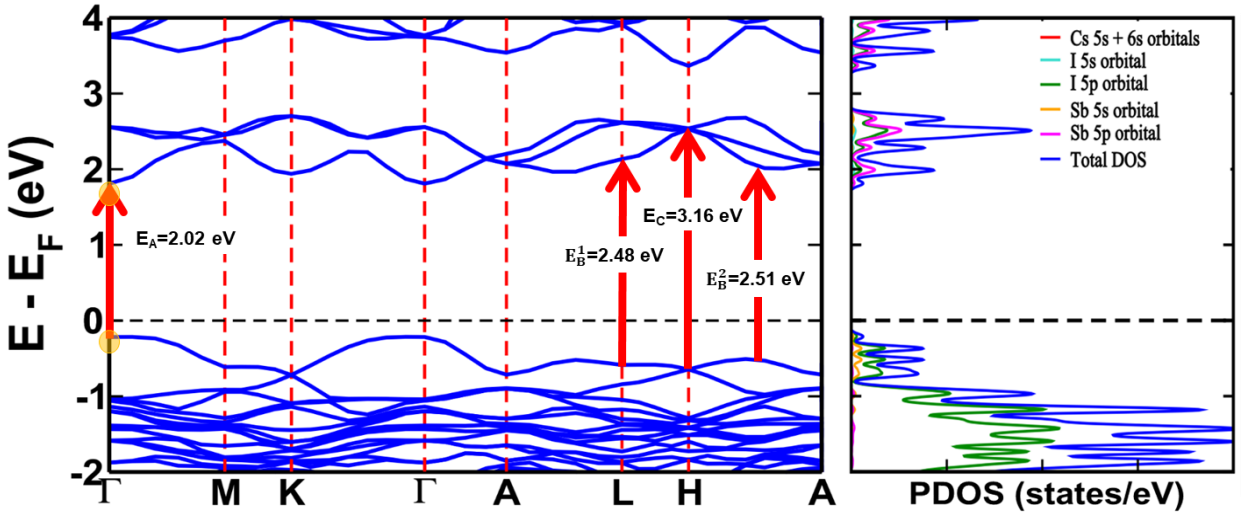

(a)

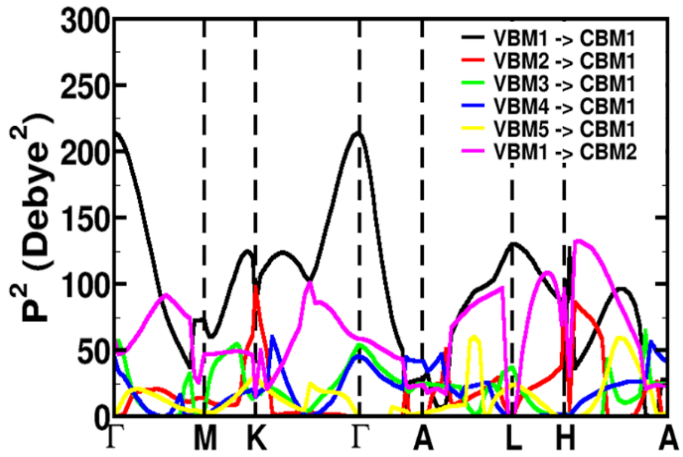

(b)

Figure 3.6 *(a) The optical transitions in the HSE06 band structure of $Cs_3Sb_2I_9$ along the high symmetry path, and (b) the band wise transition dipole moment (TDM) showing the probabilities of different transitions from several valence bands to conduction bands along the same high symmetry path.*

The different optical transitions, as shown in Fig. 3.6.(a), are as follows:

1. E_A has a value of 2.02 eV, in theory, and 2.20 eV from experiments. The transition takes place from the VBM of the highest occupied band to the CBM of the lowest unoccupied band, at the Γ point, which in fact corresponds to the band gap.
2. E_B has two possibilities in theory, one being 2.48 eV, and the other being 2.51 eV, when the experimental value is reported to be 2.60 eV. These transitions corresponding to

2.48 eV and 2.51 eV, occur from the VBM of the highest occupied band to the CBM of the lowest unoccupied band, at the L point and at a point between H point and A point, respectively. These transitions are probabilistically allowed, as seen from the TDM plot.

3. E_C has a value of 3.16 eV, in theory, and 3.34 eV from experiments. The transition takes place from the VBM of the band just below the highest occupied band to the CBM of the band just above the lowest unoccupied band, at the H point. This transition too, as it turns out, is probabilistically allowed, as seen from the TDM plot.

Our G_0W_0 calculations, as shown in figure 3.7, fit the experimental absorption spectra in a much more accurate fashion. Although, PBE functional correctly captures the peaks in the absorption spectra, it fails to reproduce the quantitative nature of the experimental plot. The G_0W_0 calculations, on the other hand, overlap well with the experimental plot.

In performing the G_0W_0 calculations, the PBE functional was considered to be a reliable starting point for our calculations. A detailed analysis has been performed over the convergence of the number of bands needed in our calculations. A study on the dependence of the quasiparticle band gap on the number of bands has been shown in Table 3.3. It can be seen that the sufficient number of bands required for calculations is 480. We have taken the number of bands to be 560 in our calculations. It is evident that the number of bands is sufficiently larger than the number of occupied orbitals.

Table 3.3 *Convergence of band gap with respect to the number of bands used in G_0W_0 calculations.*

S. No	NBANDS	Band Gap (eV)
1	240	2.03
2	320	2.03
3	400	2.03
4	480	2.04
5	560	2.04
6	640	2.04

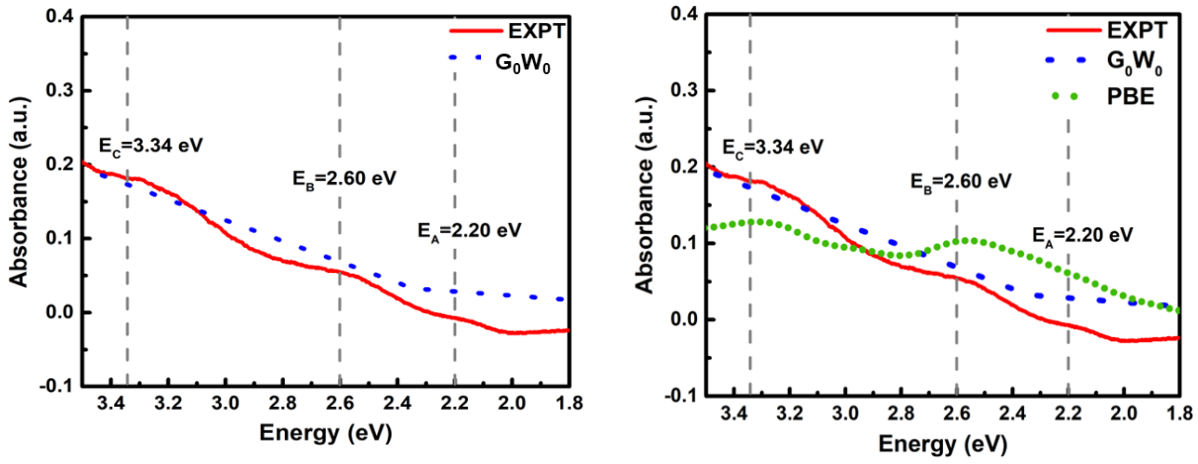

(a) (b)

Figure 3.7 *Comparison of G_0W_0 calculations with (a) experimental absorption spectrum, and (b) both experimental, and the PBE based absorption spectra.*

3.4 Conclusions

Our first-principles DFT calculations confirm that $Cs_3Sb_2I_9$ is a direct band gap semiconductor with a band gap of 2.02 eV at the Γ point (using HSE06 calculations). It is also seen that the DFT calculations do a good job in figuring out the absorption spectra when compared to experiments. We also did G_0W_0 calculations to reproduce the experimental data to a better accuracy. We identified for the first time, to the best of our knowledge, the optical transitions responsible for distinct peaks in the absorption spectra of $Cs_3Sb_2I_9$. These transitions are not only from the highest occupied band to the lowest unoccupied band, but also from states lower in energy than the highest occupied states to the states higher in energy than the lowest unoccupied state.

Bibliography

[1] Letian Dou, Yang (Micheal) Yang, Jingbi You, Ziruo Hong, Wei-Hsuan Chang, Gang Li and Yang Yang, Nat Commun. **5**, 5404 (2013).

[2] Young-Hoon Kim, Himchan Cho, Jin Hyuck Heo, Tae-Sik Kim, NoSoung Myoung, Chang-Lyoul Lee, Sang Hyuk Im and Tae-Woo Lee, Adv Mater. **27**, 1248 (2015).

[3] Guangru Li, Zhi-Kuang Tan, Dawei Di, May Ling Lai, Lang Jiang, Jonathan Hua-Wei Lim, Richard H. Friend, and Neil C. Greenham, Nano Lett. **15**, 2640 (2015).

[4] Ge Gao, Qiaoyue Xi, Hua Zhou, Yongxia Zhao , Cunqi Wu , Lidan Wang, Pengran Guo and Jingwei Xu, Nanoscale **33,** 12032 (2017).

[5] Suh-Ciuan Lim, Hsuan-Peng Lin, Wei-Lun Tsai, Hao-Wu Lin, Yao-Tsung Hsu and Hsing-Yu Tuan, Nanoscale **9,** 3747 (2017).

[6] Stefan Schünemann, Maurice van Gastel and Harun Tüysüz, Chemsuschem **13**, 2057 (2018).

[7] Yang-Fan Xu, Mu-Zi Yang, Bai-Xue Chen, Xu-Dong Wang, Hong-Yan Chen, Dai-Bin Kuang, and Cheng-Yong Su, J. Am. Chem. Soc. **139**, 5660 (2017).

[8] Sunghak Park, Woo Je Chang, Chan Woo Lee, Sangbaek Park, Hyo-Yong Ahn and Ki Tae Nam, Nat. Energy **2**, 16185 (2016).

[9] Xiaomei Wang, Hong Wang, Hefeng Zhang, Wei Yu, Xiuli Wang, Yue Zhao, Xu Zong, and Can Li, ACS Energy Lett. **5**, 1159 (2018).

[10] Akihiro Kojima, Kenjiro Teshima, Yasuo Shirai, and Tsutomu Miyasaka, J. Am. Chem. Soc. **131**, 6050 (2009).

[11] Julian Burschka, Norman Pellet, Soo-Jin Moon, Robin Humphry-Baker, Peng Gao, Mohammad K. Nazeeruddin and Michael Grätzel, Nature **499**, 316 (2013).

[12] Martin A. Green, Anita Ho-Baillie and Henry J. Snaith, Nat. Photonics **8**, 506 (2014).

[13] B. Saparov, F. Hong, J. P. Sun, H. S. Duan, W. Meng, S. Cameron et al., Chem. Mater. **27**, 5622 (2015).

[14] Y. L. Liu, C. L. Yang, M. S. Wang et al. J. Mater. Sci. **54**, 4732 (2019).

[15] G. Kresse and J. Hafner, Phys. Rev. B. **47**, 558 (1993).

[16] G Kresse and J Furthmüller, Computational materials science **6**, 15 (1996).

[17] G Kresse and J Furthmüller, Physical Review B. **54**, 11169 (1996).

[18] John P. Perdew, Kieron Burke, and Matthias Ernzerhof, Phys. Rev. Lett. **77**, 3865 (1996).

[19] John P. Perdew, Kieron Burke, and Matthias Ernzerhof, Phys. Rev. Lett. **78**, 1396 (1997).

[20] John P. Perdew, Adrienn Ruzsinszky, Gábor I. Csonka, Oleg A. Vydrov, Gustavo E. Scuseria, Lucian A. Constantin, Xiaolan Zhou, and Kieron Burke, Phys. Rev. Lett. **100**, 136406 (2008).

[21] John P. Perdew, Adrienn Ruzsinszky, Gábor I. Csonka, Oleg A. Vydrov, Gustavo E. Scuseria, Lucian A. Constantin, Xiaolan Zhou, and Kieron Burke, Phys. Rev. Lett. **102**, 039902 (2009).

[22] G. Kresse and D. Joubert, Phys. Rev. B. **59**, 1758 (1999).

[23] A. V. Krukau , O. A. Vydrov, A. F. Izmaylov, and G. E. Scuseria, J. Chem. Phys. **125**, 224106 (2006).

[24] L. Schimka, J. Harl, and G. Kresse, J. Chem. Phys. **134**, 024116 (2011).

[25] Lars Hedin, Phys. Rev. **139**, A796 (1965).

[26] Mark S. Hybertsen and Steven G. Louie, Phys. Rev. Lett. **55**, 1418 (1985).

[27] Vei Wang, Nan Xu, Jin-Cheng Liu, Gang Tang and Wen-Tong Geng, Computer Physics Communications **267**, 108033, (2021).

[28] Koji Yamada, Hiroshi Sera, Shigeko Sawada, Hironobu Tada, Tsutomu Okuda and Haruhiko Tanaka, J. Solid State Chem. **134**, 319 (1997).

[29] Mahdi Faghihnasiri, Morteza Izadifard, and Mohammad Ebrahim Ghazi, J. Phys. Chem. C, **121**, 27059 (2017).

Chapter 4

Investigations in Sliding Bilayer Graphene

4.1 Introduction

Graphite, which is one of the most prevalent carbon allotropes, is a layered material in which infinite sheets of hexagonal carbon networks are stacked over each other [1]. When isolated, a single layer is called graphene. Being sp^2 hybridized, carbon atoms in graphene are arranged in a honeycomb lattice, which is not a Bravais lattice. However, a honeycomb lattice can be viewed as a hexagonal Bravais lattice with a basis [2]. The primitive translation vectors and the carbon positions are given by [3],

$$\mathbf{a}_1 = a\left(\frac{1}{2}, \frac{\sqrt{3}}{2}\right), \quad \mathbf{a}_2 = a\left(-\frac{1}{2}, \frac{\sqrt{3}}{2}\right), \quad \mathbf{d}_1 = 0, \quad \mathbf{d}_2 = \delta = \frac{\mathbf{a}_1 + \mathbf{a}_2}{3} \tag{4. 1}$$

In graphite, the graphene layers are weakly coupled by van der Waals interactions with an equilibrium interlayer distance 3.35 Å. The minimum energy corresponds to Bernal stacking AB, and the AA stacking is energetically costly, and not found in nature [4,5]. In this work, we are interested in bilayer graphene (BLG) systems.

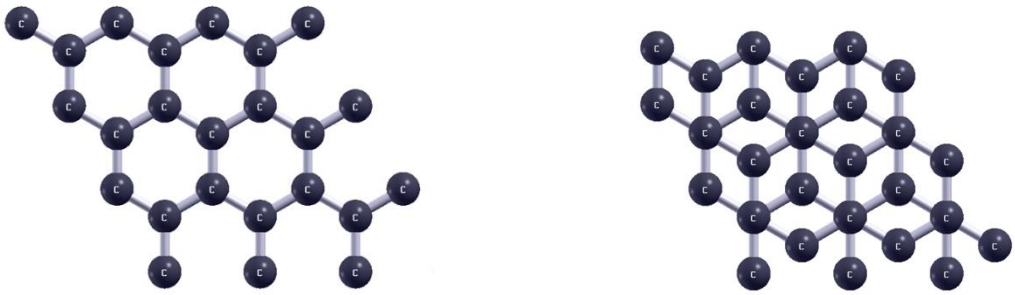

(a) (b)

Figure 4.1 *(a) AA stacked bilayer graphene and (b) AB stacked bilayer graphene.*

It is to be noted that graphene research rose considerably when graphene sheets were exfoliated for the first time in 2004 [6]. It was soon followed by the discovery of some remarkable properties of graphene sheets, which led to the explosion of interest in this field. Most interestingly, at some special high symmetry points in the reciprocal space, electrons in graphene behave as massless relativistic fermions satisfying the Dirac equation [7]. The discovery of quantum hall effect in graphene was another celebrated result in the community [8]. Furthermore, properties like high mobility of charge carriers [9], high transparency [10], and highest Young's modulus for a material ever tested [11], makes graphene a potential candidate for a large domain of applications.

Bilayer graphene too, like graphene, shares similar properties. These include high electrical conductivity [12], high thermal conductivity [13, 14], high transparency [15], and high ability to be chemically functionalized [16]. However, bilayer graphene has been shown to have massive chiral quasiparticles instead of massless Dirac fermions, as in monolayer graphene sheets [17, 18]. Very recently, bilayer graphene systems have been shown to exhibit superconductivity, when one layer is twisted with respect to the other [19, 20]. This recent addition has given more impetus to look at bilayer graphene systems, yet once again.

It is interesting to study how the various physical properties change if one of the layers slide over the other in an irrational direction. One can take the direction along y=mx, and declare 'm' to be some irrational number, in order to define an irrational direction.

4.2 Methodology

In bilayer graphene (BLG), we slide one of the layers by keeping the other fixed in a direction along the straight-line y=mx, where 'm' is some irrational number. We take m=$\frac{1}{\sqrt{2}}$, i.e., an irrational number. Now, different configurations can be made by changing the coordinates of the atoms in one of the layers by some (Δx, Δy) given by $\Delta y = \frac{1}{\sqrt{2}}\Delta x$. We choose different Δx to get different Δy. Thus, we get different configurations in BLG systems, which are denoted by α-BLG, β-BLG, and γ-BLG, for brevity.

Table 4.1 *Different configurations of bilayer graphene by sliding one layer above another.*

Δx (Crystal Coordinates)	**Δy (Crystal Coordinates)**	**Total Displacement (Crystal Coordinates)**	**Configuration Name**
0.3333	0.2356	0.4079	α-BLG
0.5000	0.3535	0.6123	β-BLG
0.6666	0.4713	0.8163	γ-BLG

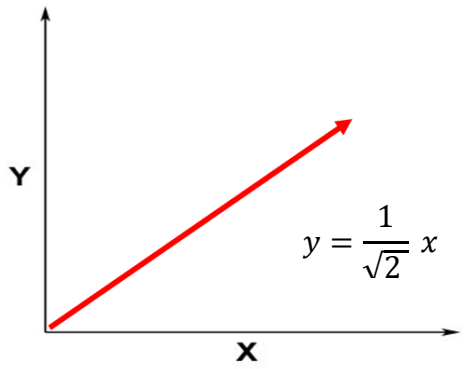

Figure 4.2 *The straight-line direction along which slide is performed.*

4.3 Computational Details

We use the plane wave basis set implementation of the density functional theory (DFT) as provided by the Quantum Espresso (QE) package [21,22] with comparative studies of both local-density approximation (LDA) [23] as parametrized by Perdew and Zunger, and generalized gradient approximation (GGA) [24] as parametrized by Perdew, Burke and Ernzerhof, to treat the exchange correlation energy functional and both projector-augmented

waves (PAW) and ultrasoft pseudopotentials to represent the interaction between ionic cores and valence electrons.

A plane wave basis set (PWs) with cut-off energy of 48 Ry was used to represent the electronic wave functions, and PWs with an energy cut-off of 480 Ry were included for the representation of charge density. Integration over the Brillouin zone was carried out using the Monkhorst-Pack scheme [25] with a 36x36x1 mesh of k points, and occupation numbers were smeared according to the Fermi-Dirac scheme with a spreading of 0.003 Ry. Kohn Sham (KS) equations were solved iteratively till the total energy was converged within 10^{-8} eV/cell. Structural relaxation was performed till the Feynman-Hellman forces on each atom were less than 10^{-3} eV/Å and each component of the stress tensor was less than 10^{-2} GPa.

Lattice-dynamical calculations (phonon spectrum) were performed within the framework of the self-consistent density functional perturbation theory [26]. Plane wave basis sets with cut-off energies of 50 and 500 Ry were used to describe wave functions and charge density, respectively. Integration over the Brillouin zone is performed using a 75x75x1 mesh of k-points. Such dense k mesh was used to keep the errors in the vibrational frequencies low. To understand detailed features of phonon spectra, force constant matrices (K) are obtained on a 4x4x1 q-point mesh. The dynamical matrices at arbitrary wave vectors are determined using Fourier transform based interpolations of force constant matrices to obtain phonon dispersion.

4.4 Results and Discussions

4.4.1 Crystal Structure

Bilayer Graphene in AB stacking configuration has a honeycomb lattice structure, which can be thought of as a hexagonal Bravais lattice with a two atom basis. It is to be noted that AB bilayer graphene is the stable configuration, and energetically favoured over the AA stacked configuration. The figure 4.3 shows the crystal structure of AB stacked bilayer graphene.

Calculations show that in-plane C-C bond length and the interlayer distance are close to experiments if the following combinations are tried

a. GGA as the approximation for the energy correlation functional with Grimme d2 van der Waals correction implemented. Both PAW and ultrasoft pseudopotentials reproduce the same results.
b. LDA as the approximation for the energy correlation functional with no van der Waals correction. Both PAW and ultrasoft pseudopotentials reproduce the same results.

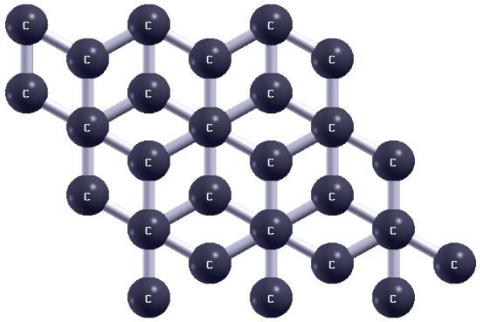

Figure 4.3 *Crystal structure of AB stacked Bilayer Graphene.*

Table 4.2 *Comparison of lattice parameters of BLG with present calculations and prior theoretical and experimental data in the literature.*

Exchange Corr Approx	**Pseudopotential**	**vdW Correction**	**C – C bond Length (Å)**	**Interlayer Distance (Å)**	**Experiments**
GGA	PAW	Grimme d2	1 .42	3.34	
		Grimme d3	1 .42	3.54	
	US	Grimme d2	1 .42	3.34	
		Grimme d3	1 .42	3.55	d_{CC} = 1.419 Å[3]
LDA		Grimme d2	1 .41	3.00	
	PAW	No vdW	1 .41	3.34	
	US	Grimme d2	1 .41	3.00	Δz_{AB} = 3.34 Å[27]
		No vdW	1 .41	3.34	

LDA functional reproduces reasonably good values for the interlayer distances without any van der Waals correction. On the other hand, one needs to incorporate van der Waals correction (more precisely Grimme d2 dispersion) for reproducing accurate interlayer distances with GGA functional. This is because LDA has a tendency to overbind [27], and therefore any further binding corrections are not needed. One can see that adding a van der Waals correction to LDA calculations further reduces the interlayer distance due to an even stronger binding.

The lattice parameters used are also given in the table below, and are in good agreement with the experimental result (*a*=2.459 Å [28]). The large c parameter has been taken to introduce vacuum into the system.

Table 4.3 *Lattice constants of BLG*

Ex Corr Approx	***a* (Å)**	***b* (Å)**	***c* (Å)**
EXPT [28]	2.459	2.459	–
GGA	2.468	2.468	16.71
LDA	2.445	2.445	16.71

It should be noted that when the different configurations are obtained by sliding a graphene layer over another, we do a constrained geometric relaxation which does not change the C-C bond length, and the interlayer distance.

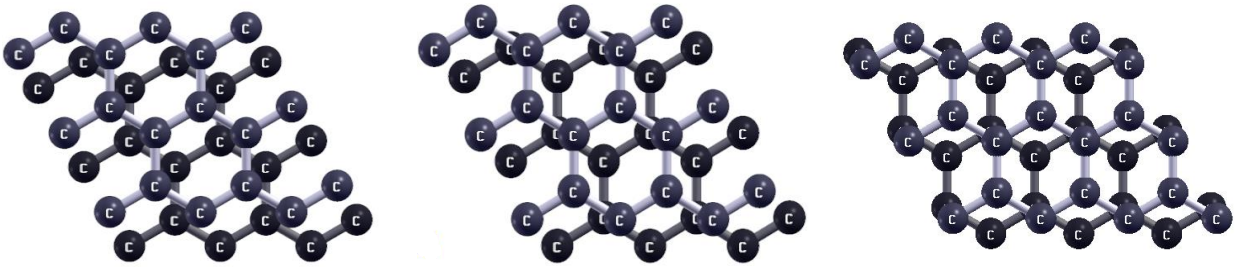

(a) (b) (c)

Figure 4.4 *(a) Configuration of α-BLG, (b) Configuration of B β-BLG, and configuration of γ-BLG.*

There is change in symmetry when one of the layers in AB stacked bilayer graphene slides over the other, which in turn has several effect on the properties of bilayer graphene. Bernal stacked graphene has $P\bar{3}m1$ space group symmetry, and the three other configurations after sliding have $P\,1^{-}$ space group symmetry. It is interesting to note that inversion symmetry is retained in all three configurations. The symmetries which are broken after sliding are:

A. A rotation of 180 degrees about [1,0,0] [0,1,0] and [1,1,0] crystal axes
B. A rotation of 180 degrees about [1,0,0] [0,1,0] and [1,1,0] crystal axes.
C. A rotation of 120 degrees about [0,0,1] and [0,0, -1] crystal axes.
D. Inversion + Rotation of 180 degrees about [1,0,0] [0,1,0] and [1,1,0] crystal axes.
E. Inversion + Rotation of 120 degrees about [0,0,1] and [0,0, -1] crystal axes.

4.4.2 Electronic Structure

Bilayer graphene has a well-known electronic band structure, which suggests that it is a zero gap semi-metal [3]. The band structures have been calculated along a high symmetry path in the reciprocal space. We have used both LDA and GGA to compare the results between the two. However, no significant difference in the band structure was observed. We selected GGA functional in conjunction with PAW pseudopotential and Grimme d2 van der Waals correction, for further calculations. We selected this scheme as it reproduced the crystal structure accurately, with the advantage of GGA functional being known to be an improvement over LDA, in general, due to the incorporation of the gradient of electron density into the functional, unlike LDA.

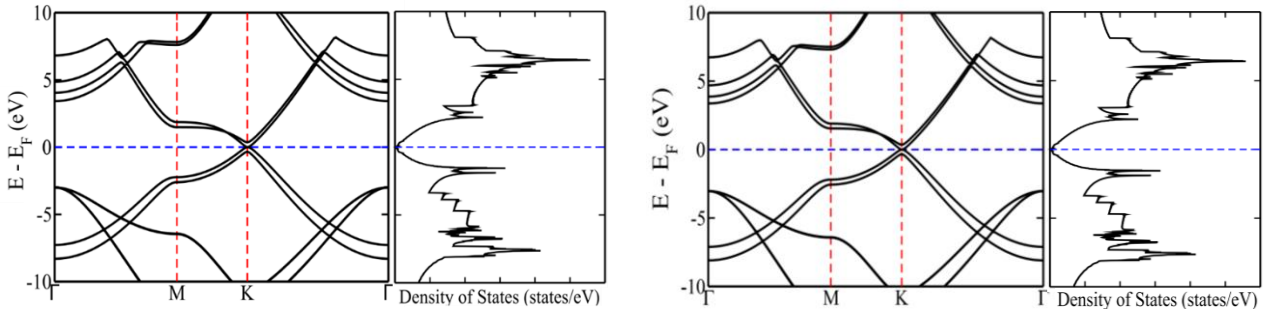

Figure 4.5 *The electronic band structure of bilayer graphene with (a) LDA functional with no vdW correction, and (b) GGA functional with Grimme d2 vdW correction, both obtained using PAW pseudopotential.*

As seen in the figure 4.5, in the low energy region, the upper half (above Fermi level) in the band structure describes parabolic unoccupied conduction bands, and the lower half (below Fermi level) describes parabolic occupied valence bands [29]. The valence bands and conduction bands touch each other at the special points called Dirac points which exist at the K (or K' by symmetry) points on corners of the Brillouin zones. The Fermi energy lies exactly at the Dirac point. This gives rise to semi-metallic behaviour. The density of states confirms the semi metallic nature of these materials.

As one slides one of the layers of bilayer graphene over the other, the band structure changes very interestingly. In the figure 4.6 given below, one can see the effects when zoomed into the low energy region near the K point. The results are summarized as follows:

a. In α-BLG, the valence bands slightly cross the Fermi level, showing metallic character.
b. In β-BLG, the valence bands just cross the Fermi level, showing a slight metallic character.
c. In γ-BLG, the valence bands and the conduction bands are separated below and above the Fermi level, and it shows a small band gap of 0.10 eV (indirect band gap).

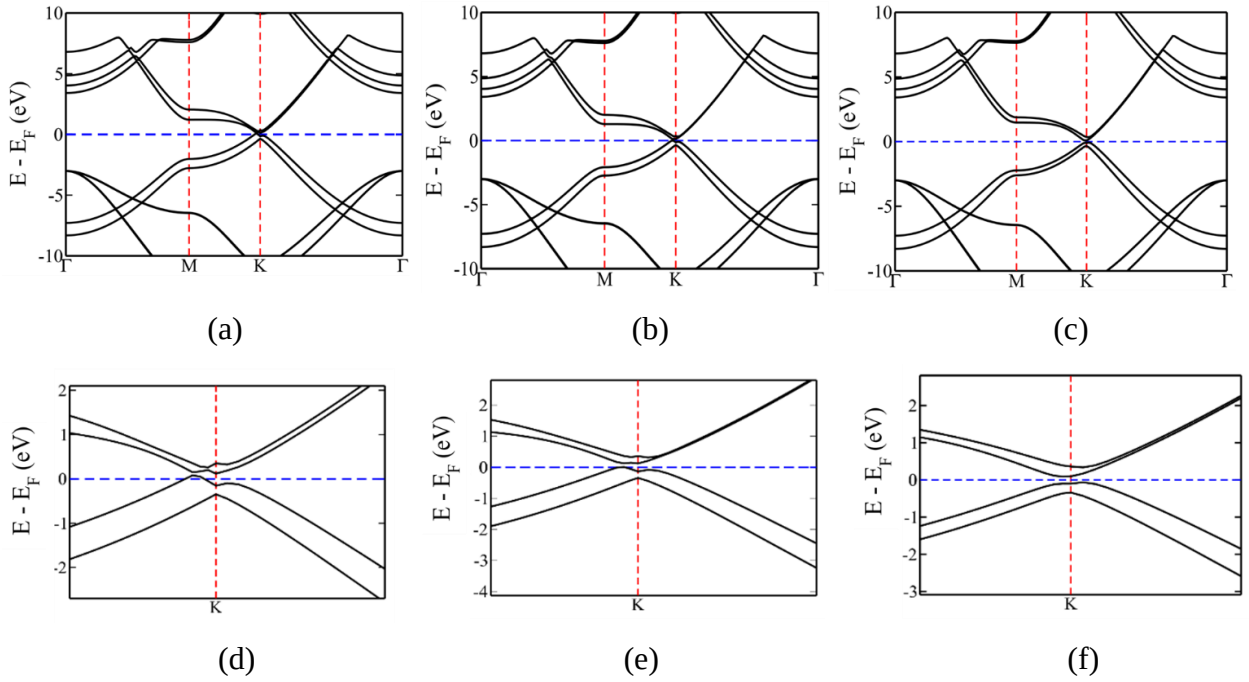

Figure 4.6 *Band structures of (a) α-BLG, (b) β-BLG and (c) γ-BLG, with zoomed in view around K point in (d) α-BLG, (e) β-BLG and (f) γ-BLG.*

The same results are confirmed by calculating the density of states of these different configurations, in figure 4.7.

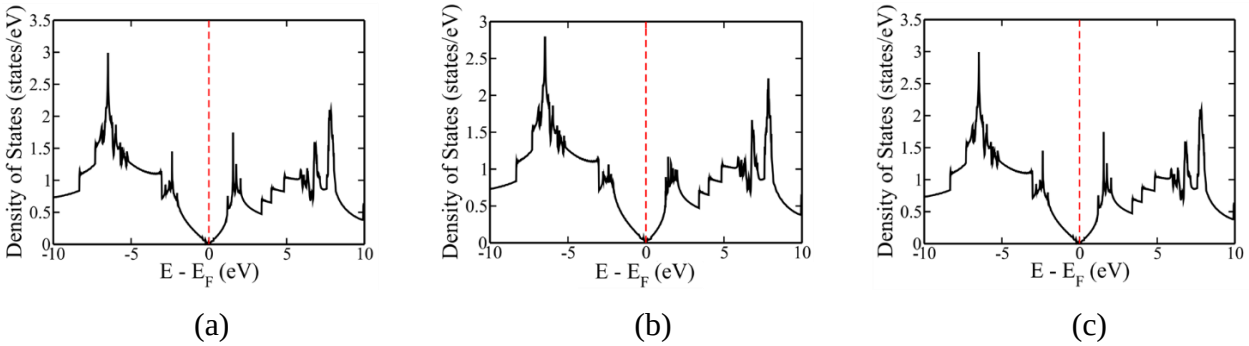

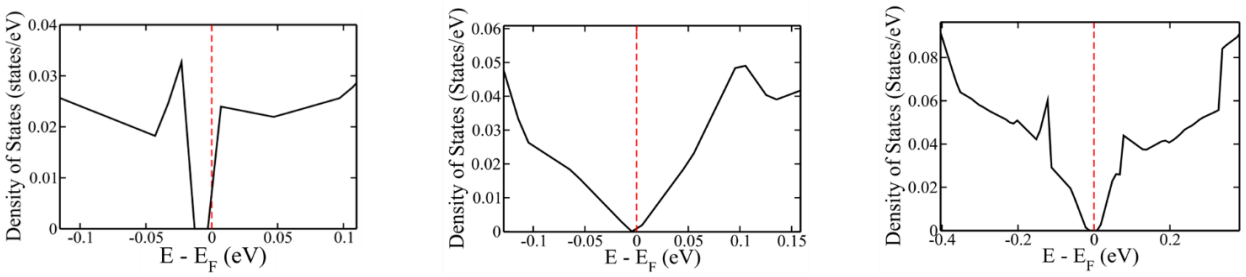

(d) (e) (f)

Figure 4.7 *Density of states of (a) α-BLG, (b) β-BLG and (c) γ-BLG, with zoomed in density of states around K point for (d) α-BLG, (e) β-BLG and (f) γ-BLG.*

The reason for such observations may be attributed to the break in symmetry in these systems, on sliding. In AB BLG, the valence band maxima (VBM) and the conduction band minima (CBM) touch each other at the K point. The VBM, and the CBM are, thus, degenerate. As one of the layers is slid over the other, the symmetry is broken, and the degeneracy is lifted. The VBM and the CBM move away from each other, and the degeneracy is lost. In both α-BLG and β-BLG, the VBM and the CBM are separated but the VBM crosses the Fermi level, indicating metallic character. In case of γ-BLG, the VBM is below the Fermi level, and the CBM is above the Fermi level, realising a band gap.

4.4.3 Vibrational Properties

The phonon dispersion spectrum is calculated using density functional perturbation theory. A detailed comparative study has been performed to detect the effects of energy cut offs and density of the K mesh used in such calculations. The effects of different approximations to the exchange correlation energy functionals like LDA and GGA, and different pseudopotentials (PAW and ultrasoft) were also studied. We choose those schemes in our calculations, which reproduced accurate crystal structures for our system. This means that when GGA was implemented, a Grimme d2 van der Waals correction was incorporated as well. For calculations using LDA, we included no van der Waals correction.

First, we performed a series of calculations by varying energy cut offs and density of the k mesh. All the results have been compared to the experimental values in graphite which also has AB stacking. We choose the LO mode, which is the highest vibrational frequency, for comparing results to experiments [32], which turns out to be around 1588 cm^{-1}.

Table 4.4 *Comparison of the phonon frequency of LO mode under the use of different exchange correlation functional approximation, pseudopotentials, energy cut offs, and k meshes.*

Exchange Correlation Approximation	**Pseudopotential**	**Energy Cut off (Ry)**	**K mesh**	**Calculated Frequency of LO mode at Γ point (in cm^{-1})**
GGA	PAW	50	50×50×1	1565
		50	75×75×1	1568
		60	75×75×1	1567
	US	50	50×50×1	1569
		50	75×75×1	1569
		60	75×75×1	1568
LDA	PAW	50	50×50×1	1605
		50	75×75×1	1604
		60	75×75×1	1604
	US	50	50×50×1	1605
		50	75×75×1	1605
		60	75×75×1	1604

It should be noted that GGA values are underestimated, and LDA values are overestimated when compared to experiments. However, in both cases, a dense k mesh gives us results close to experiments.

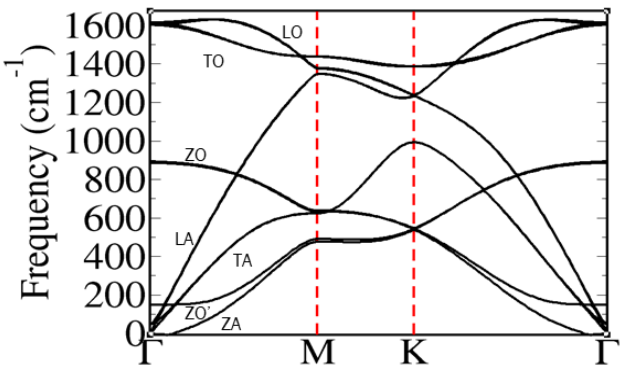

Figure 4.8 *Phonon dispersion of AB-BLG with LDA functional in conjunction with PAW pseudopotential*.

Secondly, we performed phonon calculations by taking into account different exchange correlation functionals (GGA and LDA), and pseudopotentials (PAW and ultrasoft). A Grimme d2 van der Waals correction was used for GGA, and no such correction was incorporated into LDA. A comparison was done with respect to all the phonon modes, alongside experiments [31, 32], and prior theoretical calculations [30].

We note that LDA on a whole produces phonon frequencies which are closest to prior theoretical calculations [30], and experimental results [31, 32]. GGA produces softer modes than LDA. Therefore, we selected LDA, in conjunction with PAW, to be our scheme for the next set of calculations. In fact, it is well known that LDA gives better estimation of phonon frequencies than GGA in graphitic systems [30, 33].

Table 4.5 *Comparison of phonon frequencies (in cm^{-1}) at Γ point of present calculations with prior theoretical and experimental data in the literature.*

Mode	**GGA**		**LDA**		**Theory**	**EXPT** *(Graphite)*	
	PAW	**US**	**PAW**	**US**	[30]	[31]	[32]
	Grimme d2	Grimme d2	No vdW	No vdW			
LO	1568	1569	1604	1605	1602	1583	1588
TO	1561	1563	1598	1599	1596	1577	1581
ZO	870 868	872 870	893 890	893 891	891		867 868
LA	0	0	0	0	0		0
TA	0	0	0	0	0		0
C	38	43	30	50	27		42
ZO’	45	47	76	76	75		127
ZA	0	0	0	0	0		

All the characteristic features of the phonon spectrum of bilayer graphene systems are captured by our *ab initio* calculations. Technically, we should observe twelve phonon branches as there are four atoms in the unit cell. However, we see fewer branches as some of the branches are degenerate. There are three acoustic modes, and nine optical modes.

At low q vectors, the in-plane transverse acoustic (TA) and longitudinal acoustic (LA) modes show linear dispersions, and are . The out-of-plane acoustic mode (ZA), also called the flexural

acoustic mode, shows a parabolic dispersion, denoting a characteristic feature of layered materials.

At higher frequencies, there exists out-of-plane optical (ZO) modes which correspond to interlayer motion. Due to the interlayer coupling, at the Γ point, the longitudinal optical (LO) and the transverse optical (TO) are doubly degenerate, both of which correspond to in-plane relative motion. There also exists an out-of-plane layer breathing (ZO') mode, which corresponds to an in phase out-of-plane motion of the atoms in the top and bottom layers.
At the zone centre, we get an additional doubly degenerate low frequency optical mode. It is called the shear mode and it corresponds to a shearing displacement of the atoms.

The visualization of the eigen vectors at the Γ point in figures 4.9 - 4.12 shows the different modes of vibrations which are present in this system. The carbon atoms in the different layers have been marked with different shades of blue.

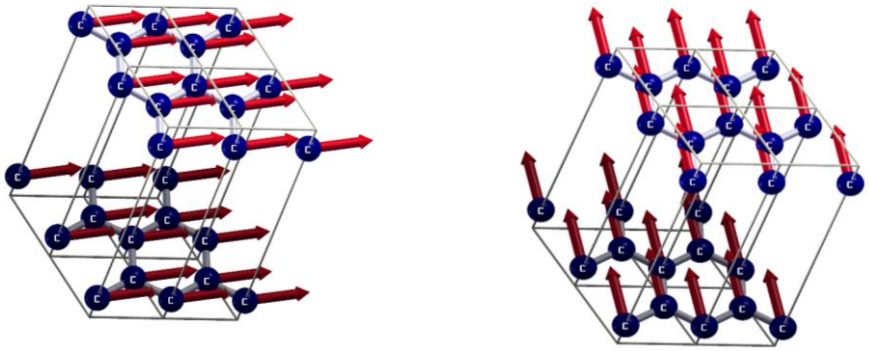

(a) (b)

Figure 4.9 *Acoustic in-plane vibrations at Γ point (a) Longitudinal Acoustic (LA) (b) Transverse Acoustic (TA) modes.*

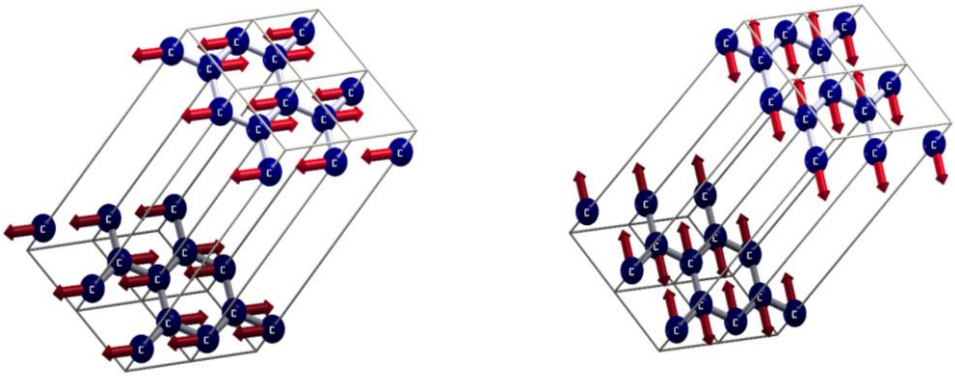

(a) (b)

Figure 4.10 *Optical in-plane vibrations at the Γ point (a) Transverse Optical (TO) (b) Longitudinal Optical (LO) modes.*

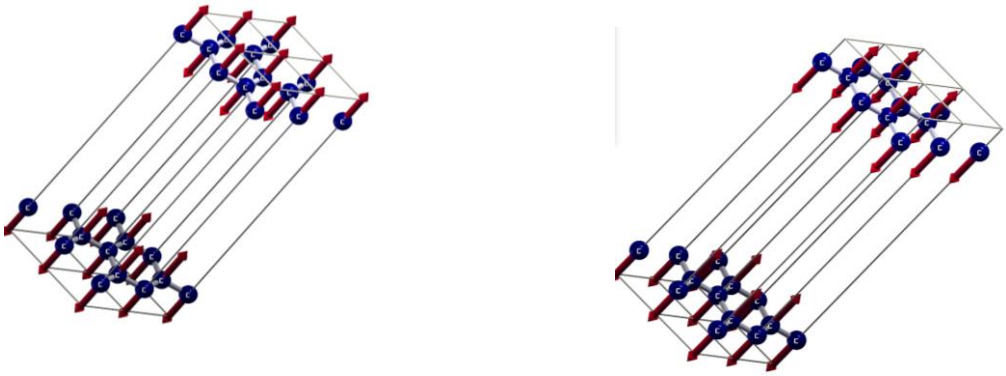

Figure 4.11 *Optical out of plane vibrations (ZO) at the Γ point.*

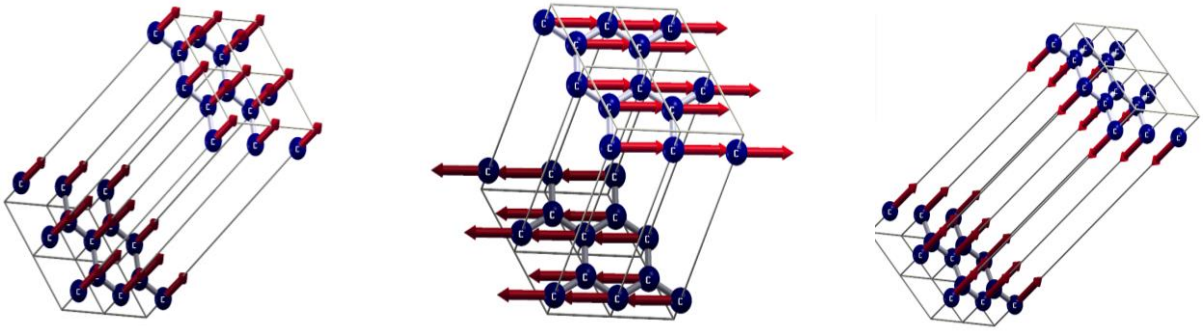

(a) (b) (c)

Figure 4.12 *(a) Flexural Mode (ZA), (b) Shear Mode (C), and (c) Layer Breathing Mode (ZO')*

The full phonon dispersion calculated using LDA gives us a fair estimate of all phonon frequencies at different high symmetry points. The qualitative nature of the phonon spectrum is well reproduced with this scheme.

Table 4.6 *Phonon frequencies (in cm^{-1}) at high symmetry points and comparison of present calculation with prior theoretical and experimental data in literature.*

Mode	**Γ**			**M**			**K**		
	Calculated	EXPT [4]	EXPT [5]	Calculated	EXPT [4]	EXPT [5]	Calculated	EXPT [4]	EXPT [5]
LO	1604	1583	1588	1374	1323	1340	1234	1194	1218
TO	1598	1565	1581	1434	1390	1399	1378	1265	-
ZO	893 890		867 868	637		630	540		542
LA	0			1348	1290	1290	1203	1194	1218
TA	0			625		628	995		1007
ZO’	76		127	479			539		542
ZA	0			474		483	539		542

When one of the layers of bilayer graphene slides over the other, the degeneracy in the frequencies of the phonon branches is lifted, and twelve distinct phonon frequencies are obtained.

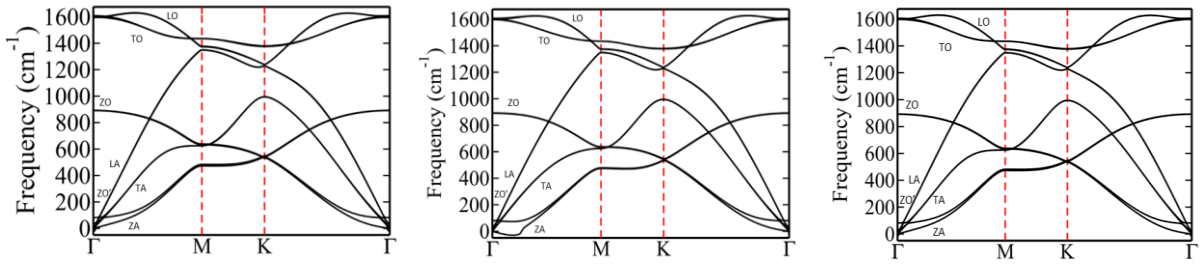

(a) (b) (c)

Figure 4.13 *Full phonon dispersion of (a) α-BLG, (b) β-BLG and (c) γ-BLG.*

BLG has four atoms in the unit cell, suggesting that there should be twelve phonon branches. However, we see fewer branches in AB-BLG, as some of the branches are degenerate. In sliding bilayer graphene, we see all twelve phonon branches due to break in symmetry.

Table 4.7 *Phonon frequencies (in cm^{-1}) of different modes, and their symmetries and Raman/IR activity at the gamma (Γ) point of α-BLG, β-BLG and γ-BLG.*

	α-BLG			**β-BLG**			**γ-BLG**		
	Frequencies (cm^{-1})	Symmetry	IR/Raman Activity	Frequencies (cm^{-1})	Symmetry	IR/Raman Activity	Frequencies (cm^{-1})	Symmetry	IR/Raman Activity
LO1	1608	Au	IR	1606	Au	IR	1599	Au	IR
LO2	1597	Ag	Raman	1597	Ag	Raman	1598	Ag	Raman
TO1	1595	Au	IR	1596	Au	IR	1607	Au	IR
TO2	1598	Ag	Raman	1598	Ag	Raman	1597	Ag	Raman
ZO1	892	Au	IR	892	Au	IR	893	Au	IR
ZO2	890	Ag	Raman	890	Ag	Raman	890	Ag	Raman
LA	0	Au	IR	0	Au	IR	0	Ag	Raman
TA	0	Au	IR	0	Au	IR	0	Au	IR
ZA	0	Au	IR	0	Au	IR	0	Au	IR
C1	-31	Ag	Raman	-21	Ag	Raman	-8	Au	IR
C2	34	Ag	Raman	29	Ag	Raman	37	Ag	Raman
ZO’	79	Ag	Raman	82	Ag	Raman	82	Ag	Raman

It should also be noted that the shear (C) modes split into two modes C1 and C2, where one of these are imaginary phonons. This can be attributed to the dynamical instability of these configurations. It is well known that AB BLG is the most stable configuration in bilayer graphene. When the one of the layers are slid over the other, there is a cost of energy that has to be overcome. Thus, α-BLG, β-BLG and γ-BLG are not the stable-most configurations. In fact, they are unstable along these shearing directions, as they have been brought into these configurations from AB BLG by sliding.

4.5 Conclusion

In conclusion, we have reported first principles density functional theory-based calculations of electronic structure and vibrational spectra of bilayer graphene, and the change in such properties change when one of the layers slides in an irrational direction. On sliding, bilayer

graphene suffers a break in symmetry from $P\bar{3}m1$ space group to $P\,1^{-}$ space group. As a result, the degeneracies in the band structure, and phonon spectra are lifted resulting in the splitting of bands in the band structure and phonon dispersion respectively. For α-BLG, and β-BLG, a metallic character is observed in the band structure, while a band gap of 0.10 eV is obtained in case of γ-BLG. The phonon frequencies split into twelve distinct modes on sliding in all α-BLG, β-BLG , and γ-BLG. One of the shear modes in these systems, is an imaginary mode which shows the dynamical instability due to the cost of energy in sliding.

Bibliography

[1] Tsuneya Ando, in *Physics and chemistry of graphene: graphene to nanographene*, edited by Enoki, Toshiaki, and Tsuneya Ando (Cambridge University Press, 2019).

[2] Mikhail I. Katsnelson and Annalisa Fasolino, in *2D Materials*, edited by Avouris, Phaedon, Tony F. Heinz, and Tony Low (Cambridge University Press, 2017).

[3] Edward McCann, and Mikito Koshino, Reports on Progress in Physics, **76,** 056503 (2013).

[4] M. Reguzzoni, A. Fasolino, E. Molinari, and M. C. Righi**,** Phys. Rev. B. **86**, 245434 (2012).

[5] G. Savini, Y.J. Dappe, S. Öberg, J.-C. Charlier, M.I. Katsnelson, A. Fasolino, Carbon **49**, 1 (2011).

[6] K. S. Novoselov, A. K. Geim, S. V. Morozov, D. Jiang, Y. Zhang, S. V. Dubonos, I. V. Grigorieva, and A. A. Firsov, Science **306**, 666 (2004).

[7] A. H. Castro Neto, F. Guinea, N. M. R. Peres, K. S. Novoselov, and A. K. Geim, Rev. Mod. Phys. **81**, 109 (2009).

[8] Yuanbo Zhang, Yan-Wen Tan, Horst L. Stormer and Philip Kim, Nature **438**, 201 (2005).

[9] K. I. Bolotin, K. Sikes, Z. Jiang, M. Klima, G. Fudenberg, J. Hone, P. Kim, H. Stormer, Solid State Commun. **146**, 351 (2008).

[10] T. Chen, Y. Xue, A. K. Roy, L. Dai, ACS Nano **8**, 1039−1046 (2013).

[11] J. U. Lee, D. Yoon, H. Cheong, Nano Lett. **12**, 4444 (2012).

[12] C. R. Dean, A. F. Young, I. Meric, C. Lee, L. Wang, S. Sorgenfrei, K. Watanabe, T. Taniguchi, P. Kim, K. L. Shepard and J. Hone, Nature Nanotech. **5,** 722 (2010).

[13] Suchismita Ghosh, Wenzhong Bao, Denis L. Nika, Samia Subrina, Evghenii P. Pokatilov, Chun Ning Lau & Alexander A. Balandin, Nature Mater. **9,** 555 (2010).

[14] Alexander A. Balandin, Nature Mater. **10,** 569 (2011).

[15] R. R. Nair, P. Blake, A. N. Grigorenko, K. S. Novoselov, T. J. Booth, T. Stauber, N. M. R. Peres and A. K. Geim, Science **320,** 1308 (2008).

[16] D. C. Elias, R. R. Nair, T. M. G. Mohiuddin, S. V. Morozov, P. Blake, M. P. Halsall, A. C. Ferrari, D. W. Boukhvalov, M. I. Katsnelson, A. K. Geim and K. S. Novoselov, Science **323,** 610 (2009).

[17] K. S. Novoselov, E. McCann, S. V. Morozov, V. I. Fal'ko, M. I. Katsnelson, U. Zeitler, D. Jiang, F. Schedin and A. K. Geim, Nature Phys. **2,** 177 (2006).

[18] Edward McCann and Vladimir I. Fal'ko, Phys. Rev. Lett. **96**, 086805 (2006).

[19] Myungchul Oh, Kevin P. Nuckolls, Dillon Wong, Ryan L. Lee, Xiaomeng Liu, Kenji Watanabe, Takashi Taniguchi, and Ali Yazdani, Nature **600**, 240 (2021).

[20] Bitan Roy and Vladimir Juričić, Phys. Rev. B. **99**, 121407(R) (2019).

[21] Paolo Giannozzi, Stefano Baroni, Nicola Bonini, Matteo Calandra, Roberto Car, Carlo Cavazzoni, Davide Ceresoli, Guido L Chiarotti, Matteo Cococcioni, Ismaila Dabo, et al. Journal of physics: Condensed matter **21**, 395502 (2009).

[22] Paolo Giannozzi, Oliviero Andreussi, Thomas Brumme, Oana Bunau, M Buongiorno Nardelli, Matteo Calandra, Roberto Car, Carlo Cavazzoni, Davide Ceresoli, Matteo Cococcioni, et al. Journal of Physics: Condensed Matter **29**, 465901 (2017).

[23] J. P. Perdew and Alex Zunger, Phys. Rev. B. **23**, 5048 (1981).

[24] J. P. Perdew, K. Burke, and M. Ernzerhof, Phys. Rev. Lett. **77**, 3865 (1996).

[25] H.J. Monkhorst and J.D. Pack Phys.Rev.B. **13**, 5188 (1976).

[26] S. Baroni, S. de Gironcoli, A. Dal. Corso, and P. Giannozzi, Rev. Mod. Phys. 73, 515 (2000).

[27] A. van de Walle and G. Ceder, Phys. Rev. B. **59**, 14992 (1999).

[28] Baskin, Y. and L. Meyer, Physical Review **100**, 544 (1955).

[29] 5 Y. H. Ho, J. Y. Wu, Y. H. Chiu, J. Wang, and M. F. Lin, Phil. Trans. R. Soc. A **368**, 5445 (2010).

[30] E.L. Silva, M.C. Santos, J.M. Skelton, Tao Yang, T Santos, S.C. Parker, A Walsh. Materials Today Proceedings. 20, 373-382 (2020).

[31] J. Maultzsch, S. Reich, C. Thomsen, H. Requardt, and P. Ordejon, Phys. Rev. Lett. **92**, 075501 (2004).

[32] M. Mohr, J. Maultzsch, E. Dobardžić, S. Reich, I. Milošević, M. Damnjanović, A. Bosak, M. Krisch, and C. Thomsen, Phys. Rev. B. **76**, 035439 (2007).

[33] Sanjeev K. Gupta, Himadri R. Soni, and Prafulla K. Jha, AIP Advances **3**, 032117 (2013).